SPATIALLY-RESOLVED NARROW LINE REGION KINEMATICS IN ACTIVE GALACTIC NUCLEI

Melissa S. Rice, Paul Martini[1], Jenny E. Greene
Harvard-Smithsonian Center for Astrophysics; 60 Garden Street, MS20; Cambridge, MA 02138

Richard W. Pogge
Department of Astronomy; The Ohio State University; 140 West 18th Avenue; Columbus, OH 43210

Joseph C. Shields
Physics & Astronomy Department; Ohio University; Athens, OH 45701

John S. Mulchaey
Carnegie Observatories; 813 Santa Barbara Street; Pasadena, CA 91101

and

Michael W. Regan
Space Telescope Science Institute; 3700 San Martin Drive; Baltimore, MD 21218
ApJ accepted [15 Sept 2005]

ABSTRACT

We have analyzed *Hubble Space Telescope* spectroscopy of 24 nearby Active Galactic Nuclei (AGNs) to investigate spatially-resolved gas kinematics in the Narrow Line Region (NLR). These observations effectively isolate the nuclear line profiles on less than 100 parsec scales and are used to investigate the origin of the substantial scatter between the widths of strong NLR lines and the stellar velocity dispersion σ_* of the host galaxy, a quantity which relates with substantially less scatter to the mass of the central, supermassive black hole, and more generally characterize variations in the NLR velocity field with radius. We find that line widths measured with STIS at a range of spatial scales systematically underestimate both σ_* and the line width measured from ground-based observations, although they do have comparably large scatter to the relation between ground-based NLR line width and σ_*. There are no obvious trends in the residuals when compared with a range of host galaxy and nuclear properties. The widths and asymmetries of [O III] $\lambda 5007$ and [S II] $\lambda\lambda 6716, 6731$ as a function of radius exhibit a wide range of behavior. Some of the most common phenomena are substantial width increases from the STIS to the large-scale, ground-based aperture and almost no change in line profile between the unresolved nuclear spectrum and ground-based measurements. We identify asymmetries in a surprisingly large fraction of low-ionization [S II] line profiles and several examples of substantial red asymmetries in both [O III] and [S II]. These results underscore the complexity of the circumnuclear material that constitutes the NLR and suggests that the scatter in the NLR width and σ_* correlation can not be substantially reduced with a simple set of empirical relations.

Subject headings: galaxies: active — galaxies: kinematics and dynamics — galaxies: nuclei — galaxies: Seyfert

1. INTRODUCTION

The width of emission lines from the Narrow Line Region (NLR) in Active Galactic Nuclei (AGNs) has recently received a great deal of interest because it may provide a reasonably accurate, although not precise, estimate of the host galaxy spheroid velocity dispersion σ_*. The NLR $\sigma_g =$ FWHM/2.354 may therefore be a reasonable 'tertiary' black hole mass $M_\bullet$ estimator based on a series of empirical relations that originate with the $M_\bullet - \sigma_*$ relationship between the mass of a galaxy's central, supermassive black hole and the stellar velocity dispersion of the host galaxy's spheroid (Ferrarese & Merritt 2000; Gebhardt et al. 2000a) and the relation between σ_* and NLR line width from Nelson & Whittle (1996, and earlier work by Whittle 1992b,c). Subsequent measurements and analysis have found that the $M_\bullet - \sigma_*$ re-

lationship has an intrinsic scatter of no more than 0.3 dex in $\log M_\bullet$ and that this upper limit is due to present measurement uncertainties (Tremaine et al. 2002). Nelson (2000) used this relation and $M_\bullet$ estimates from reverberation-mapping experiments to propose the use of σ_g measured from the [O III] $\lambda 5007$ line to estimate the black hole mass. Greene & Ho (2005) recently completed a direct comparison of σ_* and the gas velocity dispersion σ_g for approximately 2000 AGNs from the Sloan Digital Sky Survey (SDSS) and showed that these widths are well correlated, although with considerable scatter.

The empirical relation between σ_g and $M_\bullet$ is important for a broad range of applications. These applications include estimates of $M_\bullet$ for local AGNs, for AGNs at high redshift, and the cosmic evolution of supermassive black holes. For luminous AGNs with substantial continuum emission, or for AGNs at high redshift, the widths of the narrow emission lines may be the only method to determine σ_*. In conjunction with measurements of bolometric luminosity L_{bol}, estimates of $M_\bullet$

[1] Current Address: Department of Astronomy; The Ohio State University; 140 West 18th Avenue; Columbus, OH 43210; martini@astronomy.ohio-state.edu

can also be used to calculate the accretion luminosity of AGN in terms of the Eddington ratio L_{bol}/L_{Edd}. At low-redshifts, black hole estimates from reverberation mapping have been shown to agree quite well with the slope of the slope of the $M_\bullet - \sigma_*$ relation (Gebhardt et al. 2000b; Ferrarese et al. 2001; Nelson et al. 2004; Onken et al. 2004) and have been used to calibrate an additional secondary (virial) $M_\bullet$ estimator based on the line width and luminosity of the broad, permitted lines (e.g. Kaspi et al. 2000). Boroson (2003) used this virial relation to show that the [O III] FWHM could be used to estimate $M_\bullet$ to within a factor of five. The virial and σ_g estimates of $M_\bullet$ have been used to explore the black hole masses and accretion rates in particular classes of AGNs, most notably the Narrow Line Seyfert 1s (Grupe & Mathur 2004), as well as to search for evolution in the $M_\bullet - \sigma_*$ relation (Shields et al. 2003). Measurements of evolution in the $M_\bullet - \sigma_*$ relation, or skewness in the distribution of the scatter about this relation, could also provide valuable constraints on the formation history of supermassive black holes (Robertson et al. 2005).

The utility of σ_g measurements as a proxy for $M_\bullet$ in AGNs is largely limited by the substantial scatter in the relation between σ_* and σ_g. The brightest line for σ_g measurements is the [O III] $\lambda 5007$ line, although this line does suffer from substantial blue-side asymmetries (e.g. Heckman et al. 1981) that dramatically affect the quality of the $\sigma_g - \sigma_*$ correlation. Greene & Ho (2005) found that $\sigma_g/\sigma_* = 1.34 \pm 0.66$ for the full profile of the [O III] $\lambda 5007$, while after removal of the blue-side asymmetry the result for the line core is $\sigma_g/\sigma_* = 1.00 \pm 0.35$. The other bright NLR lines, [O II] $\lambda 3727$ and [S II] $\lambda\lambda 6716, 6731$, have lower ionization potentials and do not suffer from such substantial asymmetries. The scatter and quality of the $\sigma_g - \sigma_*$ relation for these lines is comparable to the core of the [O III] line. While all of these correlations do strongly confirm the Nelson & Whittle (1996) result that the kinematics of the NLR are dominated by gravity, the origin of the scatter is not clear. One potential origin of this scatter is a nonvirial contribution to the emission line widths. These contributions are clearly present in the blue-asymmetric [O III] lines, but because these asymmetries are significantly stronger in high ionization lines like [O III], compared to lower ionization lines like [S II] (e.g. de Robertis & Osterbrock 1984), there is good evidence that a range of spatial scales contribute to the observed NLR kinematics. Beyond the gas kinematics that contribute to the [O III] blue wings, any nonvirial contribution to deviations from the $\sigma_g - \sigma_*$ correlation is evidently traced equally by the low ionization [S II] lines and the core of the higher ionization [O III] line, since these features show similar scatter.

Other potential origins for the scatter in the $\sigma_g - \sigma_*$ relation include the impact of compact radio jets and tidal distortions of the host galaxies. Nelson & Whittle (1996) found that both of these quantities correlate with systematically larger σ_g at a given σ_*, although large-scale radio jets or tidal distortions are not present in most galaxies and therefore can not be responsible for the bulk of the scatter. Small-scale radio jets may play a more significant role, however, as Ho & Peng (2001) find approximately 60% of Seyfert 1 galaxies qualify as radio loud when the nuclear radio and visible-wavelength flux is isolated from host galaxy emission. Whittle (1992c) showed that the [O III] lines are significantly broader in Seyferts with linear radio morphology and high radio luminosity, which suggests radio jets can affect the NLR velocity field. The spatial distribution of the NLR gas within the bulge may also have a substantial impact on the observed value of σ_g. While the

NLR gas must approximately trace the spheroid kinematics to produce this correlation, spatially-resolved images indicate that the NLR is often approximately confined to a plane (e.g. Pogge et al. 1989b). Whittle (1992b) found that rotation does contribute to the width of the [O III] emission line, although it does not dominate. Finally, Greene & Ho (2005) investigated if host galaxy morphology, local environment, star formation rate, AGN luminosity, and Eddington ratio correlated with the observed scatter and only found evidence for systematically larger σ_g at higher Eddington ratio. While all of these investigations have determined that tidal disturbances, the presence of a radio source, rotation, and Eddington ratio contribute to the observed scatter, none of them dominate. It would be extremely valuable if the origin of the scatter in the $\sigma_g - \sigma_*$ correlation could be identified and substantially reduced, as then σ_* (and $M_\bullet$) could be estimated more precisely for AGNs.

Further information on the origin of the scatter in the $\sigma_g - \sigma_*$ correlation, as well as a more general understanding of the NLR kinematics, may be gained from a high spatial resolution study. Nearly all studies of NLR kinematics to date have employed ground-based, single-aperture measurements with aperture sizes on the order of a few arcseconds. Such aperture sizes correspond to several hundred parsecs in projection and can include most of the NLR. There is good evidence, however, for the presence of stratification in the NLR, such as observations that higher-ionization and higher critical density lines tend to be broader (de Robertis & Osterbrock 1986), the presence of a blue, asymmetric wing on the higher-ionization [O III] line and not on other, lower-ionization lines such as [S II], and evidence for modest increases in electron density from recent *HST* observations (Barth et al. 2001; Shields et al. 2005). The properties of [O III] led Heckman et al. (1981) to propose that asymmetries in the NLR are due to radial outflow and wind models of the NLR (e.g. Krolik & Vrtilek 1984; Schiano 1986; Smith 1993) are supported by recent, spatially-resolved *HST* STIS kinematics of NGC 4151 (Nelson et al. 2000; Das et al. 2005). These authors find evidence for both a rotational component and two, kinematically-distinct radial outflow components that appear to decelerate at larger scales. Crenshaw & Kraemer (2000) similarly studied the central 400 parsecs of NGC 1068 and found evidence for radial outflow driven by either wind or radiation pressure in the nuclear region, followed by deceleration on larger spatial scales.

In the present paper we analyze spatially-resolved spectroscopy of a large sample of nearby AGN from archival STIS observations and measure the NLR kinematics as a function of aperture size. We investigate the origin of the scatter in the $\sigma_g - \sigma_*$ correlation through a range of line width measurements at increasing aperture size, ranging from the limits of *HST* resolution to an aperture size typical of ground-based studies. We also study line asymmetries as a function of aperture size to investigate the spatial origin of line asymmetries. The sample properties and selection are described next in §2 and the nonstandard aspects of the data processing in §3. We describe the line width and asymmetry parameters in §4, along with the results of these measurements for different spatial scales in §5. The implications of this work for the $\sigma_g - \sigma_*$ correlation and the kinematics of the NLR are then presented in §6. We summarize our results in the final section.

2. THE SAMPLE

We have adopted the sample of Nelson & Whittle (1995, hereafter NW95) as the parent sample of this investigation of small-scale NLR kinematics because they have obtained high-

quality ground-based measurements of many NLR emission features, as well as stellar velocity dispersions, for a wide range of galaxy types. Their sample is largely drawn from the 140 Seyfert galaxies discussed in Whittle (1992a), where their primary selection criteria was for strong Mg b ($\sim$5175Å) and Ca II triplet ($\sim$8550Å) absorption features and weak Fe II emission (which confuses Mg b). With moderate spectral resolution (80–230 km s^{-1} FWHM) they measured the redshift, stellar kinematics (V_* and σ_*), and a variety of characteristics for the [O III] λ5007 and [S II] λ9096 lines (see §4). These high-quality ground-based data are a critical point of comparison for our study of the small-scale kinematics.

We searched the *HST* archive and found 24 AGNs from the NW95 sample with moderate-resolution spectroscopy of either the [O III] or [S II] emission lines (G430M and G750M gratings, respectively) through either an 0.1″ or 0.2″ wide slit. The spectral resolution of the G750L and G430L gratings ($\sim$500 km s^{-1}) is not high enough to resolve line width changes in nearly all of these sources, while in contrast the instrumental resolution is substantially higher for G430M and G750M. The 0.1″ and 0.2″ slit widths have a spectral resolution of $\sim$ 1.5 pixels FWHM for point sources and the G430M and G750M gratings have dispersions of 0.28 and 0.56 Å/pixel. The instrumental velocity resolution FWHM is therefore 25 and 40 km s^{-1}, respectively. The resolution is approximately a factor of $\sim$ 2.7 times larger for an unresolved source that uniformly fills the 0.2″ slit and a factor of $\sim$ 1.7 times larger for the 0.1″ slit. The STIS plate scale is 0.05078″ per pixel and the slit length is 50″. The details of our sample, including host galaxy properties, program ID, and observing mode, are provided in Table 1. Of the 24 galaxies, only NGC 2110 has observations with both the G430M and G750M settings.

3. DATA REDUCTION

Our sample is drawn from many different STIS observing programs and thus the objects were obtained with many different observing sequences. The reduction steps therefore vary from galaxy to galaxy depending upon the number of dithered exposures, the number of CR-split frames, and if the observations were obtained prior to the primary (Side 1) STIS electronics failure on 2001 May 16. We found that the reduced spectra taken directly out of the CALSTIS pipeline are not of optimum quality for any of our galaxies. In this section we discuss our modifications to the CALSTIS pipeline for the various observing sequences employed to obtain these archival data.

3.1. *Multiple Dithered Exposures*

Twelve of our 24 galaxies (those obtained for proposals 7361, 8055, and 9143) include multiple exposures of the nucleus and employed integer pixel dithering along the slit. These exposures had only one CR-split frame, and thus the CALSTIS pipeline reduction did not include cosmic ray correction. To account for the cosmic rays, we broke out of the CALSTIS pipeline after the dark-subtraction, bias-subtraction, and flat-fielding for each exposure (using the _flt.fits calibration file). After aligning the exposures, we used the Laplacian Cosmic Ray identification IRAF routine (L.A. Cosmic; van Dokkum 2001) to create a bad pixel map for each 2-D spectrum. The pixels flagged as cosmic rays by L.A. Cosmic were then rejected when the multiple spectra were combined. L.A. Cosmic occasionally mistook spectral

features for cosmic rays, leaving emission lines blank in the final combined image. In these cases we replaced the empty pixels with the corresponding values from the original _flt image. Once the cosmic-ray cleaning was complete, we re-inserted this combined, cosmic ray-rejected file into the CALSTIS pipeline for the final wavelength and flux calibrations.

3.2. *Multiple CR-splits*

When multiple images were obtained at the same pointing, the exposures could be combined with the `ocrreject` step in the CALSTIS pipeline to produce a cosmic ray corrected image. We have run the spectra from galaxies with multiple CR-splits listed in Table 1 up through this cosmic ray rejection step in the CALSTIS pipeline. However, even with multiple CR-splits, the pipeline output most often is still peppered with cosmic rays. We thus used L.A. Cosmic to zap the remaining rays in the ocrreject output (_crj.fits image) before re-inserting the spectra into the pipeline for the wavelength and flux calibrations.

3.3. *Side 2 STIS Electronics Correction*

The ten datasets for proposal 9143 were obtained after 2001 May 16, when the Side 1 STIS electronics failed. The Side 2 electronics do not have closed-loop temperature control of the CCD and this results in a dark rate that varies with temperature. Thus the dark calibration image is a poor approximation to the real dark rates for hot pixels and the outputs of the CALSTIS pipeline have many strongly negative pixels after the dark-subtraction step. Unfortunately, even the dithering scheme employed for this proposal did not easily remove the negative 'holes' created in the images.

To correct for these negative pixels, we roughly followed the method outlined by Pogge et al. (2005, *in preparation*). From the combined, cosmic ray-rejected image for each galaxy (see §3.1), we created a list of pixels that fell more than 3-σ below the background median, which we fed into a custom IRAF script that replaced each negative pixel with the mean of its surrounding 3×3-pixel box. We then re-inserted this corrected image into the CALSTIS pipeline. For images obtained prior to the Side 1 electronics failure, hot pixels that remained after the dark correction were eliminated as part of the cosmic ray cleaning step.

4. DATA ANALYSIS

Once these steps were complete, we extracted 1-D spectra of different aperture sizes from the 2-D spectra using the CALSTIS `x1d` routine, which performs a geometric rectification and background subtraction. For each galaxy we extracted spectra with apertures of integer pixel sizes from 2–50 centered on the nucleus, corresponding to angular sizes of 0.10″ − 2.54″. We chose to integrate progressively wider apertures, rather than attempt to measure the differential line profiles as a function of radius, because one of the main goals of our study is to characterize the transition between NLR profiles on very small scales and the ground-based apertures used in previous work.

Figure 1 presents three 1-D spectra for each of the 24 galaxies in the sample. The leftmost column of panels plots each galaxy's spectrum summed over an 0.2″ aperture, which approximately represents the nuclear emission unresolved by STIS. The middle column of panels plots the sum of a 1″ aperture centered on the nucleus. The 1″ aperture was chosen as a compromise between the resolution of previous ground-based studies and the angular extent over which emission lines

TABLE 1
OBSERVATION AND SAMPLE PROPERTIES

Name	Class	cz (km s^{-1})	Dist. (Mpc)	D (")	Morph. (T)	log$L_{1.4GHz}$ (W/Hz)	ID	Mode	CR-SPLIT	Apertures (")	Refs. Dist.	Refs. D	Refs. Morph.
(1)	(2)	(3)	(4)	(5)	(6)	(7)	(8)	(9)	(10)	(11)	(12)	(13)	(14)
MKN 270	2	3137	38.1	65.8	-2	21.51	9143	G750M	1	52X0.2	1	1	3
MKN 573	2	5166	68.9	101.9	-1	21.56	9143	G750M	1	52X0.2	4	2	3
MKN 686	2	4251	56.7	90.8	5	22.51	9143	G750M	1	52X0.2	4	2	1
NGC 788	2	4061	54.1	77.3	0	- - -	9143	G750M	1	52X0.2	4	2	3
NGC 1052	2	1307	18.0	77.3	-5	- - -	7403	G750M	3	52X0.2	2	1	3
NGC 1358	2	4008	53.4	119.7	0	- - -	9143	G750M	1	52X0.2	4	1	3
NGC 1667	2	4547	60.6	53.5	5	- - -	9143	G750M	1	52X0.2	2	1	3
NGC 2110	2	2249	30.0	42.5	-3	- - -	8610	G750M	6	52X0.2	4	2	3
NGC 2273	2	1929	27.6	203.3	5	21.84	9143	G750M	1	52X0.2	1	1	1
NGC 3031	1.8	-39	1.4	1439.3	3	20.81	7351	G750M	2	52X0.1	1	1	3
NGC 3227	1.5	1024	20.6	119.7	1	21.84	7403	G750M	2	52X0.2	1	1	3
NGC 3516	1.5	2503	38.9	137.5	-2	21.85	8055	G750M	1	52X0.2	1	1	3
NGC 3982	2	1155	17.0	109.2	3	21.54	7361	G750M	1	52X0.2	1	1	3
NGC 4051	1.5	622	17.0	361.5	4	21.35	8228	G750M	1	52X0.2	1	1	3
NGC 4579	1.9	1334	19.1	378.6	3	21.34	7403	G750M	3	52X0.2	3	1	3
NGC 5347	2	2295	31.1	101.9	2	21.07	9143	G750M	1	52X0.2	1	1	3
NGC 5427	2	2733	33.2	181.2	5	- - -	9143	G750M	1	52X0.2	1	1	3
NGC 7682	2	5109	68.1	65.8	2	22.59	9143	G750M	1	52X0.2	4	1	3
MKN 348	2	4505	60.1	75.5	0	22.17	8253	G430M	2	52X0.2	4	2	3
MKN 1066	2	3523	47.0	72.1	-5	23.16	8253	G430M	2	52X0.2	4	2	3
NGC 2110	2	2249	30.0	42.5	-3	- - -	8253	G430M	2	52X0.2	4	2	3
NGC 4151	1.5	966	20.3	424.8	2	22.25	8473	G430M	3	52X0.2	1	1	3
NGC 5194	2	461	7.7	534.8	4	22.20	7574	G430M	2	52X0.2	1	1	3
NGC 5929	2	2250	38.5	65.8	2	22.22	8253	G430M	2	52X0.2	1	1	3
NGC 7674	2	8673	115.6	60.0	4	23.63	8259	G430M	2	52X0.2	4	1	3

REFERENCES. — Distances: (1) Tully (1988); (2) Jensen et al. (2003); (3) Solanes et al. (2002); (4) $H_0 = 75$ km s^{-1} Mpc^{-1} (adopted for consistency with Tully (1988)). Size and Morphology: (1) Nilson (1973); (2) Vorontsov-Velyaminov & Arkipova (1974); (3) de Vaucouleurs et al. (1991)

NOTE. — Col. (1): Galaxy name. Several common aliases are MKN 270 = NGC 5283, MKN 686 = NGC 5695, NGC 3031 = M81, and NGC 5194 = M51a. Col. (2): AGN type, where Type 1 AGN exhibit broad permitted lines and Type 2 AGN have narrow permitted lines. Col. (3): [O III] profile median redshift from Nelson & Whittle (1995) ([O III] C80 or [S III] C80 redshifts used for galaxies with no [O III] median redshift given). Col. (4): Distance. Col. (5): Angular diameter in arcsec of the 25 mag arcsec^{-2} isophote. Col. (6): Morphological type (de Vaucouleurs numerical type). Col. (7): Radio luminosity (log$_{10}$ of the absolute spectral luminosity at 1.4GHz) from Condon et al. (2002). Col. (8): *HST* proposal ID for data used. Col. (9): STIS grating. Col. (10): Number of CR-split exposures. Col. (11): STIS aperture. Cols. (12)–(14): References to published distances, sizes and morphologies.

are detectable in most of the STIS spectra. Finally, the rightmost column of panels shows the difference of the middle and leftmost panels. The difference spectra in these panels thus illustrate the line profiles *outside* of the nucleus and will be discussed below in the context of line widths and asymmetries outside of the nuclear region.

We applied a scalar throughput correction to the flux-calibrated 0.2″ spectra (4-pixel extraction box height) produced by x1d because the default throughput correction table (referenced by the PCTAB keyword) does not include an entry for a 4-pixel extraction box height. When a 4-pixel extraction box height is requested, the throughput value for a 3-pixel box height is employed instead by default, although the throughput is approximately 10% larger for a 4-pixel box compared to a 3-pixel box. The default behavior of x1d therefore overestimates the flux in a 4-pixel box when it assumes the lower throughput appropriate for a 3-pixel box. To properly correct the 0.2″ spectra, we interpolated the throughput values in the correction table to calculate the appropriate quantity for a 4-pixel box height for each instrument configuration and then applied this throughput correction to the x1d output. Also, we note that while the throughput correction in the table was calculated from observations of a point source, the AGN in this sample are dominated by unresolved nuclear emission and this correction table is a reasonable approximation. This throughput correction is only relevant to the 1″−0.2″ and 0.2″ spectra shown in Figure 1 because the correction is negligible at 1″. The correction also does not affect the width measure-

ments because the spectra are only multipled by a constant.

We have chosen to characterize the line profiles of the [O III] and [S II] emission lines as a function of aperture size through line widths measured at a range of heights, intercentile velocity widths (IPVs), and asymmetry measures (e.g. Heckman et al. 1981; Whittle 1985a). The definitions of these parameters, our measurement procedure, and their physical motivation, are discussed in detail below. The measurements of each of these quantities are listed in Tables 3 and 4 for 0.2″ and 1″ apertures. We present an illustration of these parameters in Figure 2.

4.1. *AGN Continuum Subtraction*

The first step in measurement of the [O III] and [S II] line profiles is accurate subtraction of the continuum. This is particularly important for characterization of any broad wings on the line profiles. In all cases, we defined continuum regions approximately 300–600 km s^{-1} away from the lines under consideration. For all but four of our targets (NGC 3227, NGC 3516, NGC 4051, and NGC 4579), we found that the faint AGN continuum was well-approximated by a constant over this narrow wavelength range. For these four bright galaxies, we had sufficient signal-to-noise ratio in the continuum to justify a power-law fit. The STIS slit size is sufficiently narrow that no significant stellar features appear to contaminate the continuum.
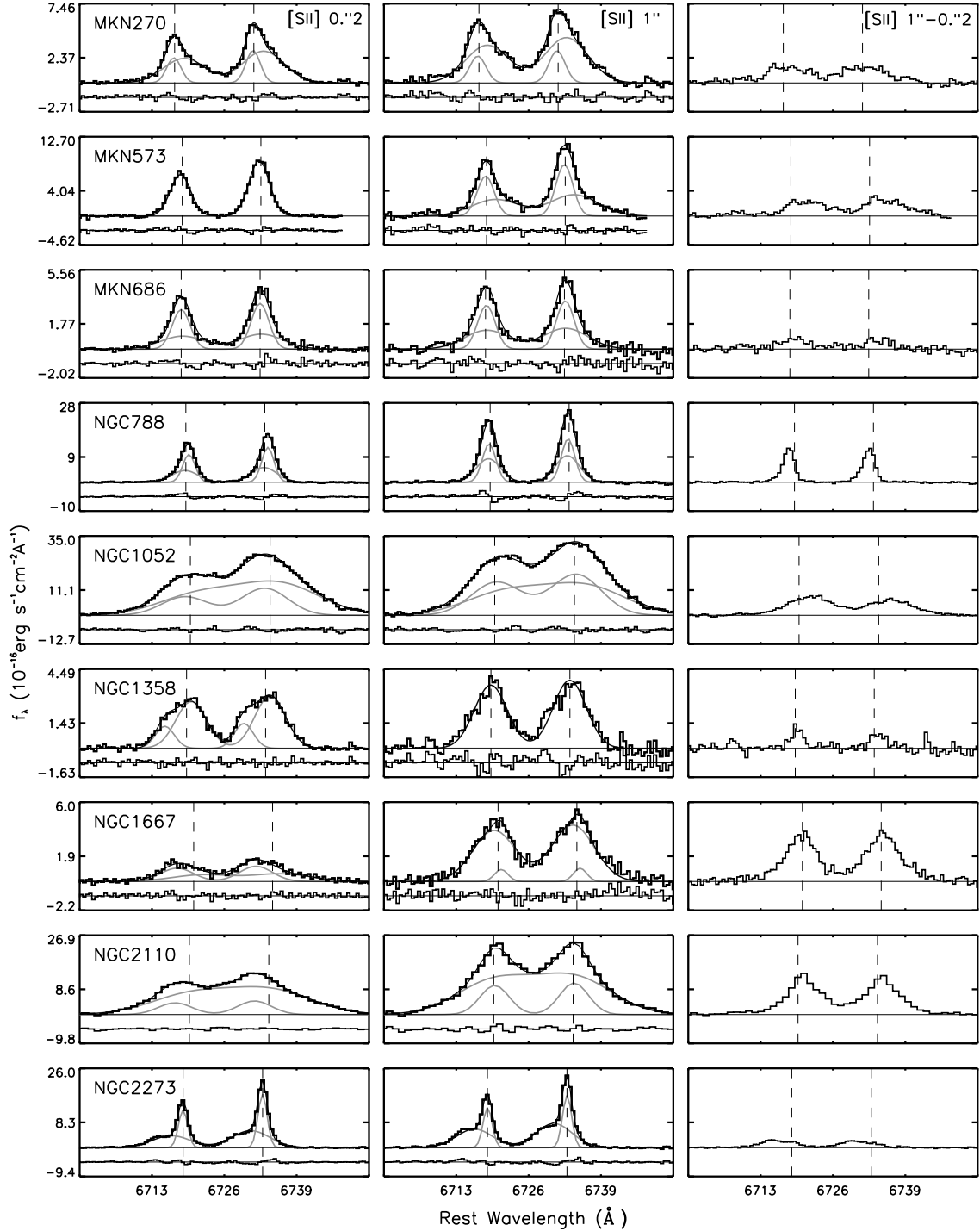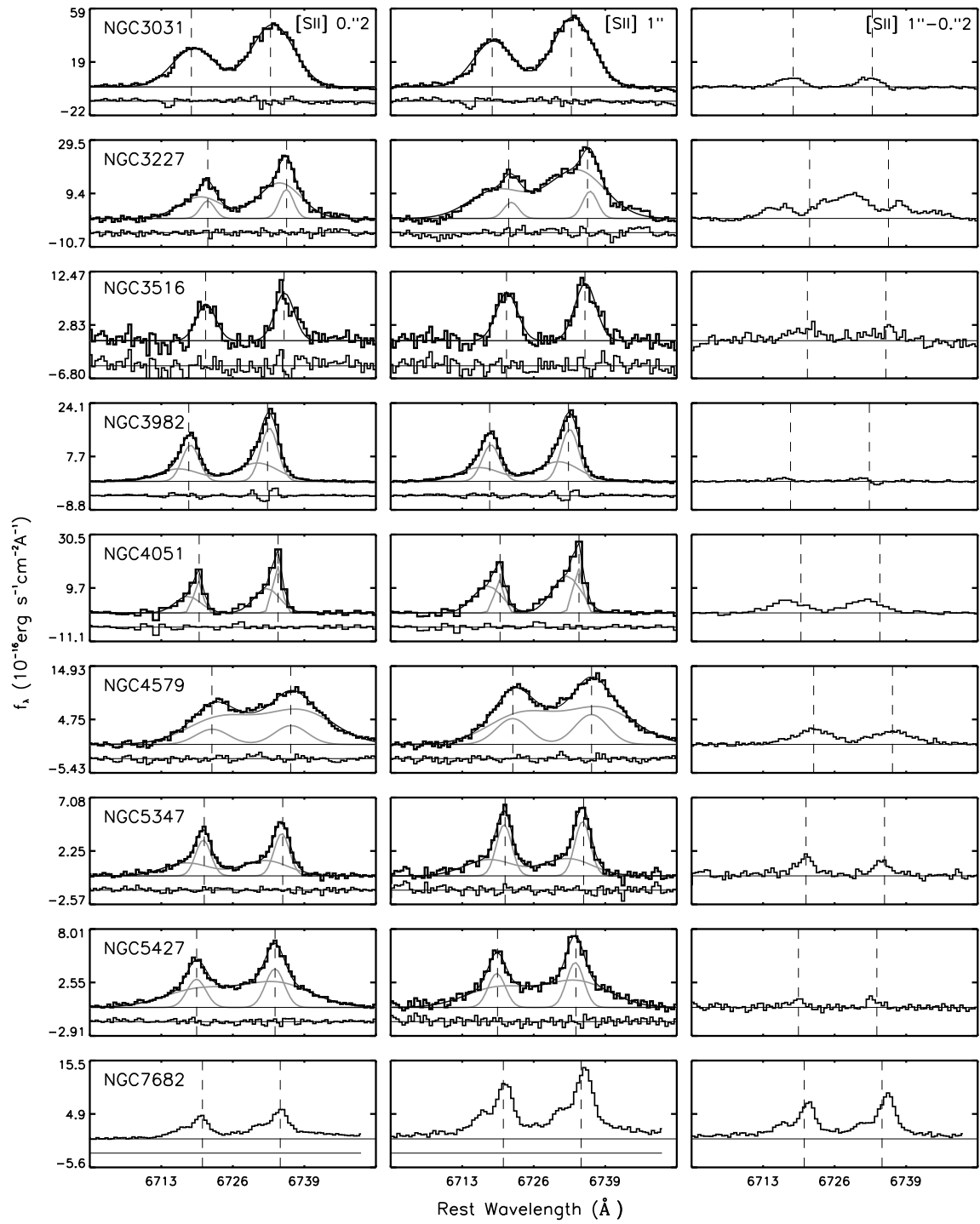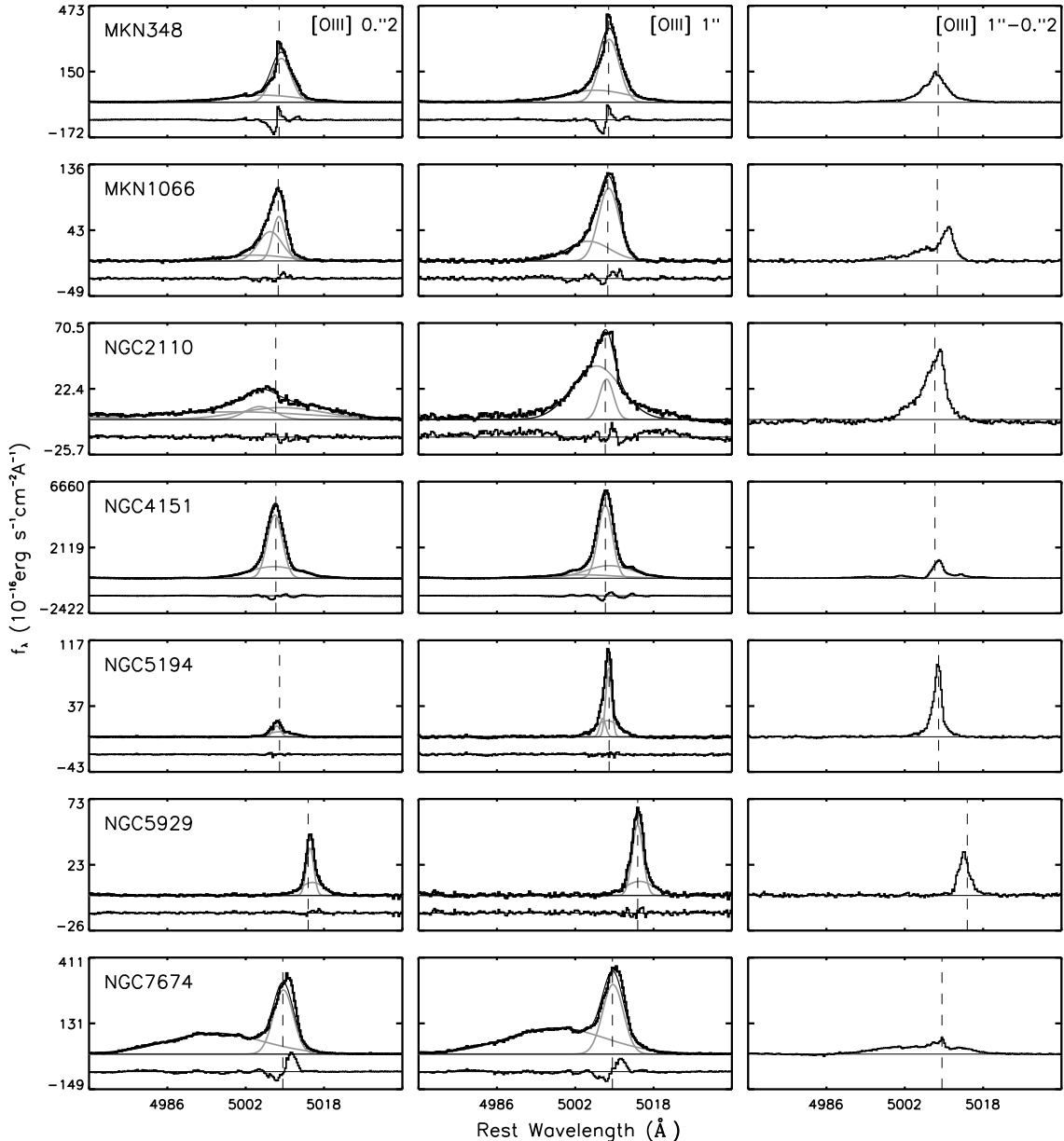
4.2. *Line Width Measurements*

FIG. 1.— Profiles for the [S II] λλ6717,6731 or [O III] λ5007 lines for our sample are presented at aperture sizes of 0.2″ (left column) and 1″ (middle column), as well as for 1″ − 0.2″ (right column). The best fit Gaussian profiles are shown as smooth, solid lines, while the individual components are shown as grey lines. Residuals are plotted below each fit. The vertical dashed line represents the position of the centroid of each line profile in the 1″ aperture. A polynomial fit to the AGN continuum has been subtracted from NGC 3227, NGC 3516, NGC 4051, and NGC 4579. All other profiles have only had a constant subtracted. The profiles have been plotted in rest wavelengths using the cz values from in Table 1. Note that a Gaussian profile was not fit to NGC 7682 because the STIS G750M grating was centered too far to the blue and the broad, red wing of the [S II] λ6731 line did not fall on the detector.

FIG. 1.— *Continued*

FIG. 1.— *Continued*

We have characterized the mean velocity structure in the [O III] $\lambda\lambda4959, 5007$ and [S II] $\lambda\lambda6717, 6731$ emission lines through measurement of FW20, FWHM, and FW80, which are the line widths at 20%, 50%, and 80% of the peak height, respectively. These parameters, as illustrated in Figure 2, yield the base widths, core widths, and top profile widths described in Heckman et al. (1981). We have linearly interpolated the flux between wavelength bins (~ 0.28Å for the G750M and G430M gratings) to measure the widths. The value FWHM/2.354 was used for comparison with the stellar velocity dispersion measurements measured by Nelson & Whittle (1995).

Several of the AGNs have sufficiently blended [S II] lines such that the flux between the 6717Å, 6731Å doublet exceeds the 20 percent peak value for both lines. For the most severely blended of these, the FWHM value was undefined as well, and for NGC 1052 and NGC 2110 the FW80 value could

not be measured. We find that the [S II] lines often become more blended with increasing aperture size and for several galaxies the FW20 and FWHM measurements become undefined above some aperture size. In these cases we measured the width values from a Gaussian fit to the line profile (our Gaussian fitting scheme is described in §4.3). Table 1 lists our width measurements of [S II] and/or [O III] for each of the sources at aperture sizes of 0.2" and 1.0" and indicates the values obtained from a Gaussian fit (with a *g* superscript). Figure 3 shows the value of these three quantities as a function of aperture size.

These width measurements are the observed widths and have not been corrected for the instrumental resolution. As noted in section 2, the FWHM velocity resolution of the G430M and G750M gratings are ~ 25 and 40 km s^{-1}, respectively, for an unresolved point source and a factor of up to ~ 2.5 times higher for a source that fills the slit. The most commonly used method to correct for broadening due to the
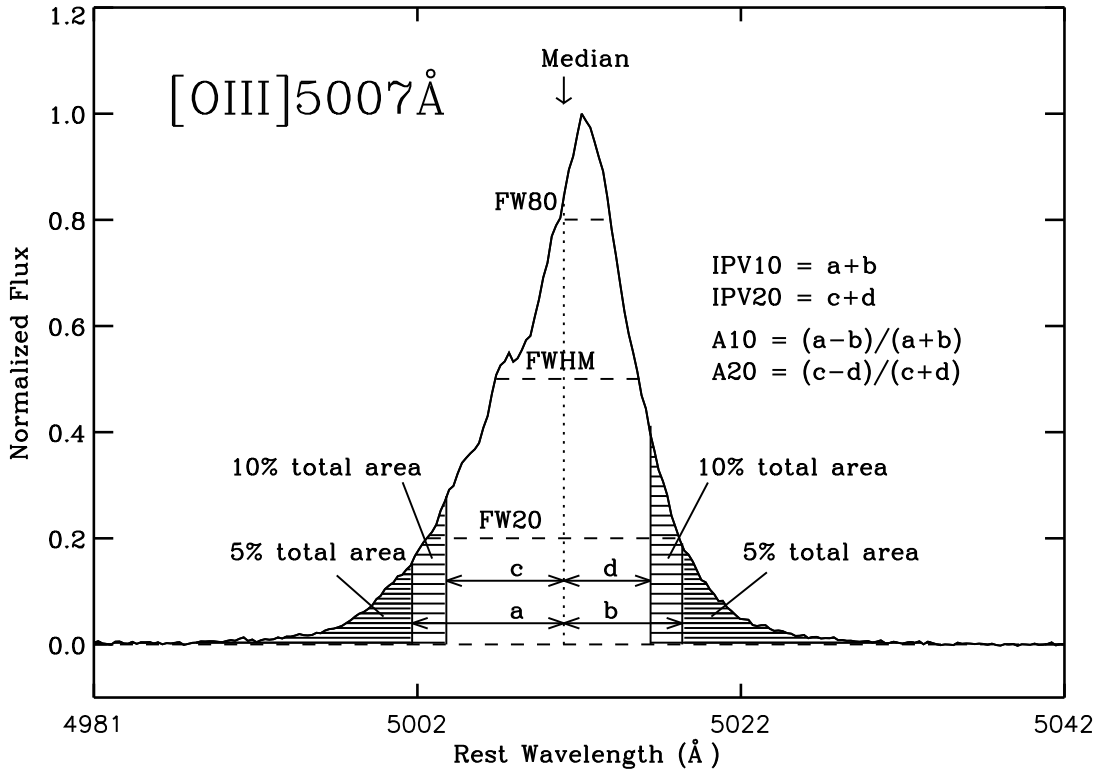
FIG. 2.— A sample [O III] λ 5007 profile (0.2″ aperture) with definitions of the width parameters FW20, FWHM, FW80, IPV10, and IPV20, and the asymmetry parameters A10 and A20. Note the broad wings and blue asymmetry typically seen in AGN [O III] profiles.

instrumental resolution is to subtract the width of the instrumental resolution in quadrature. This correction is can not be performed with great accuracy for these observations because there is a substantial difference in resolution between unresolved and resolved emission and both sources of emission likely contribute to the observed emission line profile. However, we can estimate the magnitude of this effect for the narrowest lines in our sample, which have FWHM $\sim$ 120 km s^{-1} (see Table 1), and represent the most affected measurements. If this emission were completely unresolved the correction would be less than 5% and if it uniformly filled the slit it would be less than 30%. Because the two-dimensional spectra of these sources all indicate that the emission-line gas is centrally peaked, we estimate that the majority of the emission in the smallest aperture is still unresolved. We therefore conclude that instrumental resolution makes at most a small contribution to our reported line widths. For the majority of our sample, the line widths are sufficiently broad that this correction is less than 10% even with the most extreme assumption that the emission uniformly fills the aperture. We also note that the instrumental resolution correction is likely to be more important for the line core (FW80) than at smaller fractions of the peak height (e.g. Whittle 1985a).

In their study of 1749 AGNs spectra from the SDSS, Greene & Ho (2005) found that the moments of Gaussian fits to the profiles provide more robust widths than direct measurements from the spectra. However, the SDSS data are typically lower signal-to-noise ratio (SNR) and width measurements can be more uncertain in the low SNR regime. The STIS spectra used for our sample generally have sufficient SNR and resolution that we can confidently measure emission line widths without assuming any model for the line shape. Also, because

the majority of the line profiles have a blue or redshifted wing and/or a broad central component, measuring widths directly from the data allows us to avoid approximating single values of the moments from a combination of multiple Gaussian components.

The dominant uncertainty in direct measurement of the line widths is the continuum level because these lines have high signal-to-noise ratio. As noted above in Section 4.1, we fit the continuum by either a constant or a power law. The line width measurement uncertainty depends on both the uncertainty in the continuum level and the line profile shape, as for example a given continuum uncertainty will produce a smaller width uncertainty in a broad line than a narrow line. We estimate that the uncertainties in our direct width measurements are less than 5%. The width measurements that required Gaussian fits have a formal uncertainty of approximately 5% (Greene & Ho 2005), although this is only a true estimate if the lines can be correctly represented by Gaussians. Those cases where the fitting routine varied between direct width measurements and Gaussians (the switch between black and gray symbols in Figure 3) indicate that the uncertainties are at most 10%. The lack of substantial stellar continuum emission in the extremely narrow STIS slit removes a potentially significant source of the uncertainty in width measurements based on ground-based observations, which may be particularly relevant for fainter emission lines such as [S II].

4.3. Area and Asymmetry Measurements

Whittle (1985a) advocates the use of area measurements to define line width parameters, rather than simple cuts at varying heights, because they have an integral nature and are thus smoothly defined and less sensitive to the presence of
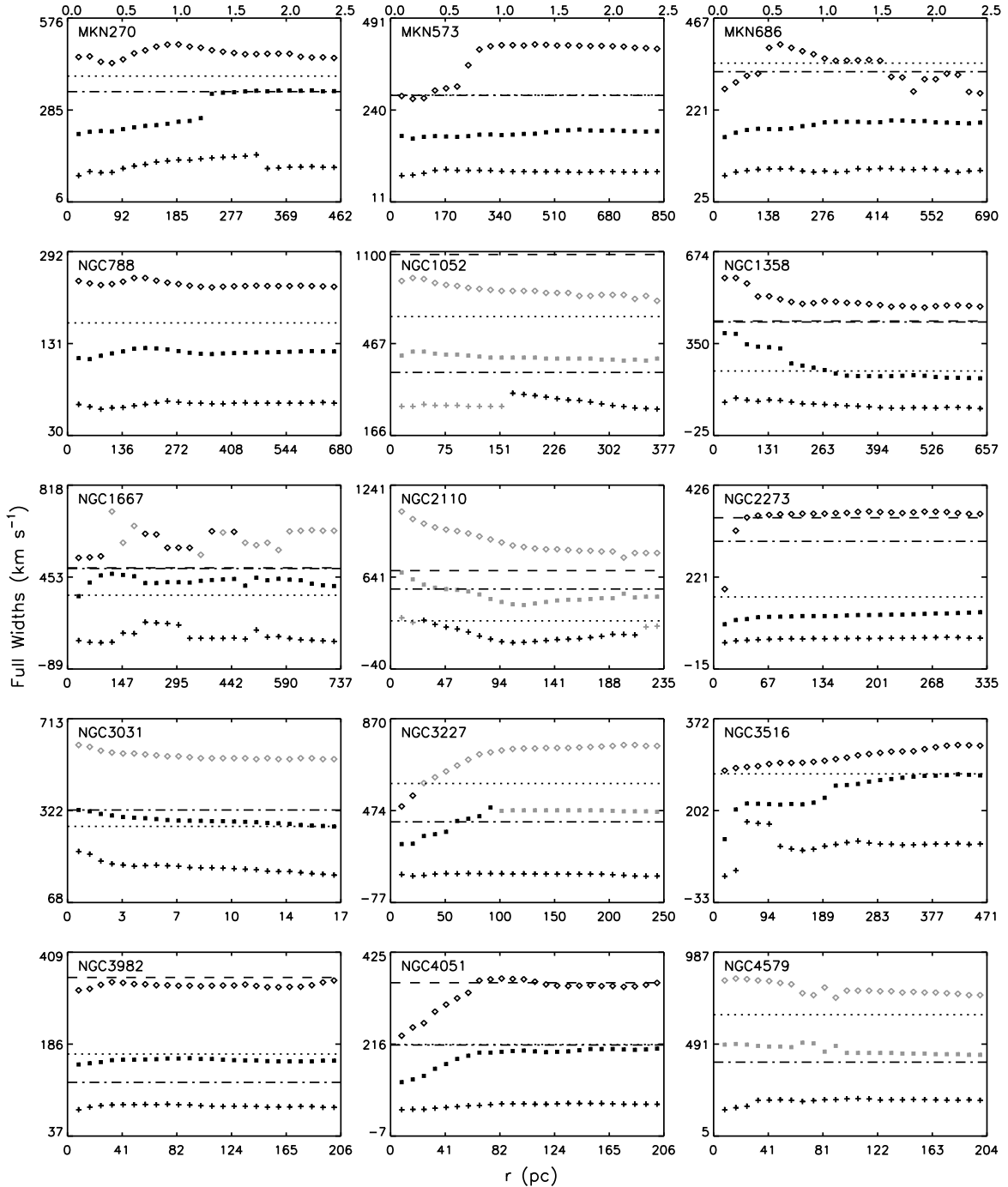
FIG. 3.— Line width parameters FW20 (diamonds), FWHM (squares), and FW80 (crosses) are plotted against aperture size in units of physical distance (below) and angular size (above) for each galaxy in our sample. The NW95 measurements for FW20 (dashed), FWHM (dotted), and 2.354 × σ_* (dash-dotted) are plotted as horizontal lines. Black symbols denote measured widths, while gray symbols denote values obtained from a Gaussian model of the line profile.

noise or the effects of instrument resolution. His definitions of the interpercentile velocity widths (IPV10 and IPV20) and asymmetries (A10 and A20) are also illustrated in Figure 2. The median is the wavelength that denotes the center of area for the profile, and the lengths a, b, c, and d represent the separation between the median and the profile's 10%, 90%, 20%, and 80% area values, respectively. The IPV10 parameter characterizes the base and wings of the profile, much as did the FW20 width suggested by Heckman et al. (1981), while the IPV20 parameter and higher percentage areas character-

ize the line core. The A10 and A20 values serve to clearly quantify the profile's red or blue asymmetry.

We have chosen to measure our area parameters from Gaussian fits to the line profiles, rather than directly from the data as discussed in Whittle (1985a). This choice was driven by the [S II] lines, which are mildly to severely blended in all of our sources. Because these lines are blended, we could not measure the interpercentile markers in the same manner as Whittle (1985a) for the more isolated [O III] λ5007 line. We experimented with taking the 10 and 20 percentile mark-
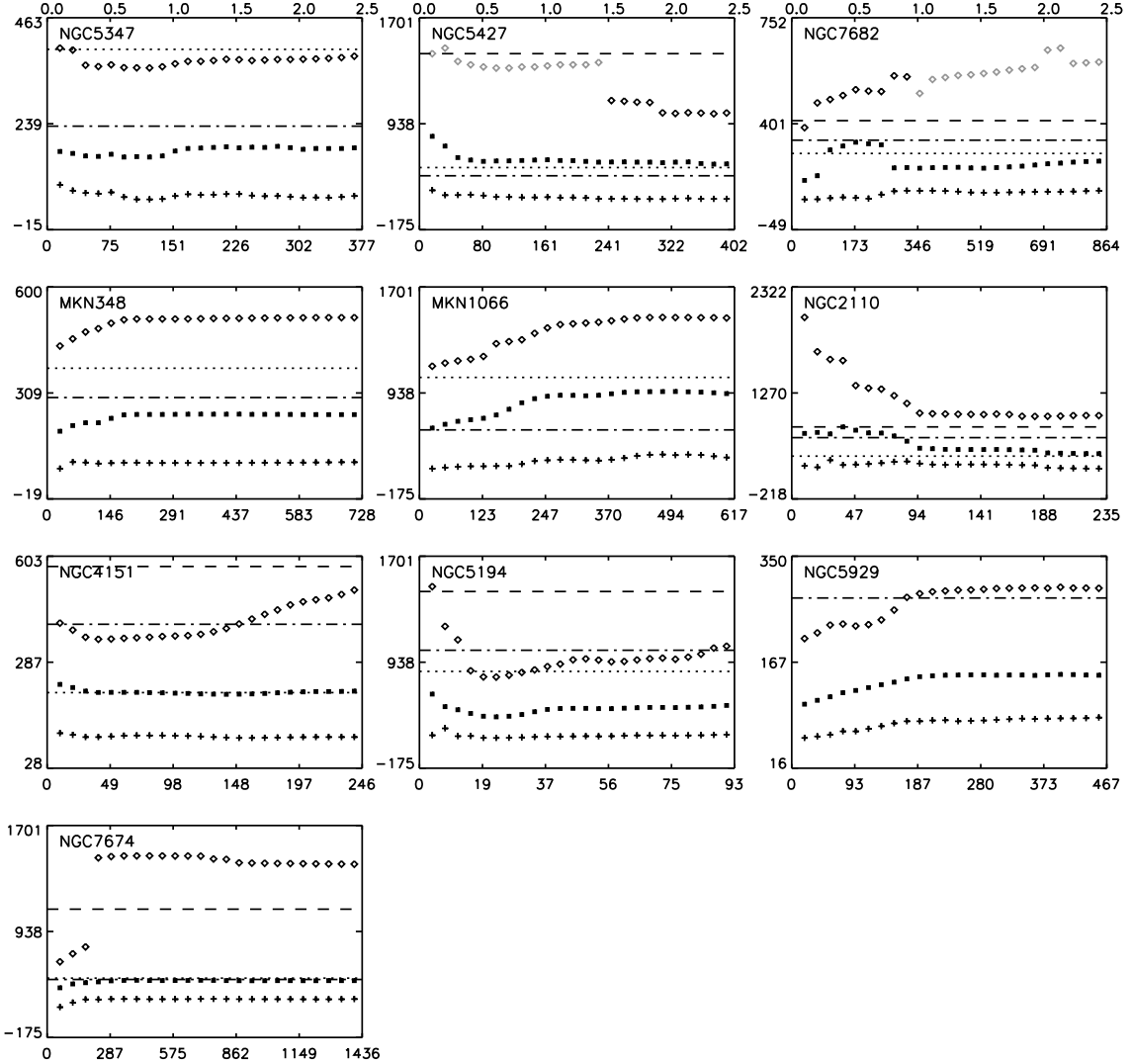
FIG. 3.— *Continued*

ers of the total [S II] doublet area from the blue wing of the 6717Å line, and the 80 and 90 percentile markers from the red wing of the 6731Å line, and then scaling the widths a, b, c and d by the relative widths of the [S II] lines, but the potentially variable line ratio of the [S II] doublet made this approach uncertain. In the end, we found that the Gaussian profiles provided more robust measurements of the area parameters, as we were able to isolate the separate contributions to the line profile from each of the [S II] lines. Also, the Gaussian fits allowed us to avoid the subtleties in treating fractional wavelength increments discussed by Whittle (1985a).

Very few of these galaxies are well fit by a single Gaussian. The [O III] line often has an asymmetric blue wing in addition to a broad central component, and so we allow for up to three Gaussian components in our fitting routines. With the exception of the sources with bright AGN continua, we fit a constant continuum term. We fit the [O III] $\lambda\lambda$4959 and 5007 lines simultaneously with their wavelength separation and relative strengths fixed to the theoretical ratio of 3:1 determined by atomic physics. For the [S II] doublet we also fit the two lines simultaneously and with a fixed separation, although we allow their relative line strengths to vary because the [S II]

λ6717/λ6731 ratio is sensitive to electron density. In principle, the line widths of the 6717Å and 6731Å lines may be different due to stratification in the NLR, so we initially allowed the widths of the two lines to vary in our fitting routine. However, we found that the widths of the two lines differed by less than 3%, which is within the error of the Gaussian fit parameters described in the previous section. We therefore fixed the widths of these two lines in the fitting routine.

The fitting routine employed here was adopted from Greene & Ho (2005). The first step is to fit a single Gaussian to the profile, and then we allow a second central component centered between -5Å and +5Å of the line peak (although occasionally the component was best fit outside these limits). We keep this second component if the χ^2 value for the fit improves by at least 20%. For [O III] we experimented with a third, blue component that was generally centered between -20Å and 0Å of the central component. Again we kept this component when χ^2 improved by at least 20%. For the [S II] lines we only allowed for one additional component between -10Å and +10Å of the line peak. The best fits from our Gaussian routine for each forbidden line profile are shown in Figure 1 and the fit residuals are plotted below the spectrum in

TABLE 2
LINE WIDTH MEASUREMENTS

Name	σ_* (km/s)	Nelson & Whittle (1995) Line	FWHM (km/s)	FW20 (km/s)	Aperture = 0.2″ Line	FW80 (km/s)	FWHM (km/s)	FW20 (km/s)	Aperture = 1″ FW80 (km/s)	FWHM (km/s)	FW20 (km/s)	1″/0.2″ (%)	NW95/1″ (%)
(1)	(2)	(3)	(4)	(5)	(6)	(7)	(8)	(9)	(10)	(11)	(12)	(13)	(14)
MKN 270	148	[O III]	396	620	[S II]	100	223	457^g	135	254	494^g	14	56
MKN 573	123	[S III]	290	540	[S II]	81	176	280	91	186	420	5.7	56
MKN 686	144	[O III]	359	609	[S II]	97	192	313	99	216	370	13	66
NGC 788	140	[O III]	190	295	[S II]	70	140	247	77	150	246	7.1	27
NGC 1052	207	[O III]	770	1085	[S II]	314^g	592^g	966^g	314^g	612^g	901^g	3.4	26
NGC 1358	173	[O III]	220	410	[S II]	117	361	574	92	224	486	-38	-1.8
NGC 1667	173	[O III]	275	410	[S II]	43	337	462	128	339	509	0.6	-19
NGC 2110	220	[O III]	295	645	[S II]	284^g	584^g	1005^g	149^g	426^g	842^g	-27	-31
NGC 2273	124	[S III]	158	348	[S II]	52	102	317	58	112	358	9.8	41
NGC 3031	167	[O III]	335	- - -	[S II]	238	388	614^g	196	355	581^g	-8.5	-5.6
NGC 3227	144	[S III]	536	1151	[S II]	59	225	473	71	395^g	708^g	76	36
NGC 3516	235	[O III]	250	550	[S II]	37	171	263	91	197	279	15	27
NGC 3982	62	[O III]	203	358	[S II]	95	184	335	100	194	341	5.4	4.6
NGC 4051	88	[S III]	208	353	[S II]	56	126	248	69	191	363	52	8.9
NGC 4579	170	[O III]	653	1278	[S II]	156	497^g	847^g	199	456^g	799^g	-8.2	43
NGC 5347	93	[O III]	392	677	[S II]	73	159	393	61	165	360	3.8	140
NGC 5427	74	[O III]	264	620	[S II]	103	282	641^g	96	232	576^g	-18	14
NGC 7682	123	[S III]	239	363	[S II]	66	155	431	98	183	466^g	18	31
MKN 348	118	[O III]	363	660	[O III]	89	195	448	86	228	506	17	59
MKN 1066	105	[O III]	417	714	[O III]	124	265	463	148	356	578	34	17
NGC 2110	220	[O III]	295	645	[O III]	161	575	1546	209	394	855	-31	-25
NGC 4151	178	[S III]	233	575	[O III]	118	246	403	116	231	387	-6.1	0.9
NGC 5194	102	[S III]	195	364	[O III]	75	120	291	57	115	205	-4.2	70
NGC 5929	121	[O III]	405	576	[O III]	66	123	230	90	160	292	30	153
NGC 7674	144	[O III]	350	960	[O III]	133	298	566	164	328	1430	10.1	6.7

NOTE. — Col. (1): Galaxy name. Col. (2): Stellar velocity dispersion measurement from NW95. Col. (3) Line used for width measurements in NW95. Cols. (4)–(5): FWHM and FW20 values from NW95. Col. (6): Line used for our width measurements. Cols. (7)–(9): Our FW80, FWHM, and FW20 measurements in an 0.2″ aperture (the g superscript denotes measurements obtained from a Gaussian model of the line profile). Cols. (10)–(12): FW80, FWHM, and FW20 values measured in a 1″ aperture. Col. (13): The percent change in FWHM between the 0.″2 to 1″ aperture sizes. Col. (14): The percent change between our 1″ FWHM measurement and the NW95 value.

each panel. The IPV at 0.″2 and 1″ are provided in Table 1 and plotted as a function of aperture size in Figure 4, while the asymmetry measurements are listed in Table 1 and shown in Figure 5. Unlike the width measurements, the IPV area-defined parameters are relatively insensitive to instrumental resolution (Whittle 1985a).

5. RESULTS

All but three of the 24 galaxies in the sample have measurable emission outside of a central, 0.2″ aperture, where 0.2″ corresponds to 8 – 115 parsecs for this sample (excluding the very nearby NGC 3031). The three galaxies that lack detectable emission outside of 0.2″ (MKN 686, NGC 3516, and NGC 5427) were observed with G750M and not G430M. The brighter [O III] line is always detectable outside of the central 0.2″. The presence of significant emission outside of 0.2″ is illustrated in the rightmost columns of Figure 1, which displays the difference between the sum of a 1″ and 0.2″ aperture centered on the nucleus. In addition to the three galaxies that do not exhibit detectable emission outside of 0.2″, nine additional galaxies with [S II] observations have weak emission on larger scales and six have substantial emission. However, even emission lines that are quite weak outside of 0.2″ can contribute to the line profiles in larger, integrated apertures.

5.1. Line Widths vs. Aperture Size

The line width and IPV values as a function of aperture size are shown in Figures 3 and 4, respectively. Figure 3 plots the radial dependence of FW20, FWHM, and FW80 for each galaxy, while Figure 4 shows IPV10 and IPV20. The figures

also include the ground-based measurements from NW95 as horizontal lines, unless the values measured in the ground-based aperture fall outside the range of the vertical axes. Our measurements in 0.2″ and 1″ apertures, along with the NW95 data, are listed in Tables 1 and 1. For nearly all of the galaxies there are substantial differences between the values in the nuclear region and the maximum STIS aperture size, as well as between the maximum STIS aperture size and the NW95 measurements. These differences between the STIS apertures and the ground-based measurements could be due to uncertain resolution corrections in the narrowest lines, although galaxies with narrow emission lines are not systematically more different than galaxies with well-resolved lines. An alternate explanation is that these measurements fall below those from NW95 because the STIS slit only subtends a fraction of the NLR. We will discuss this point further in Section 6.

Figure 3 shows that the line profile widths almost always increase or remain approximately constant. The FWHM for ten galaxies increases by greater than 10%, while for an additional 11 the FWHM changes by less than 10%. Only three galaxies decrease by greater than 10% from the 0.2″ to 1″ aperture (NGC 1358, NGC 5427, and NGC 2110 in both emission lines). Two galaxies (NGC 1358 [S II], NGC 2110 [O III]) decrease by more than 30% and are interesting cases because a decrease requires both significant emission at larger spatial scales and a velocity width that is substantially narrower at larger scales than in the nuclear region. Comparison of the 0.2″ and 1″ apertures clearly indicates that the profiles are substantially broader in the central region.

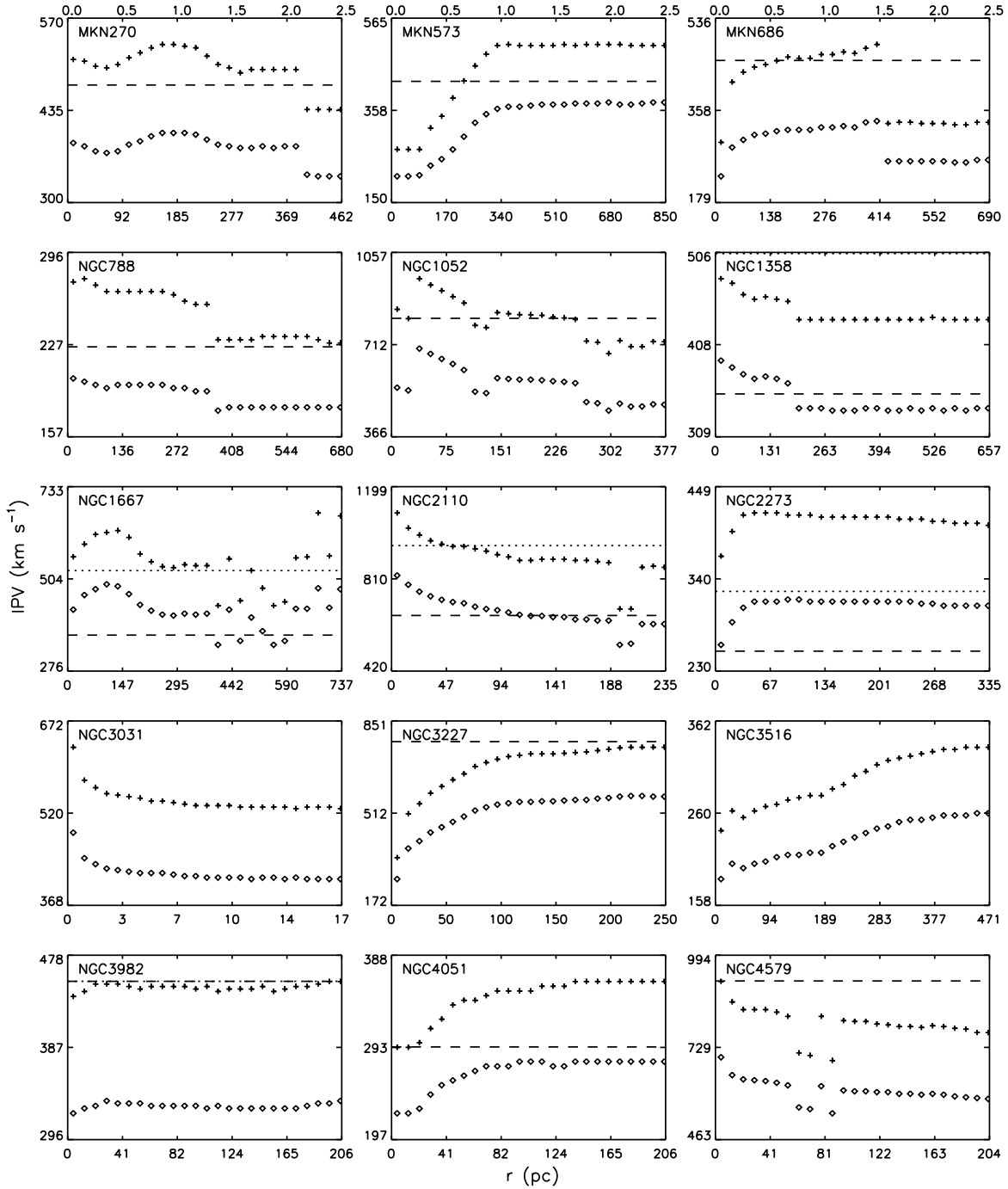IPV variations with aperture size are particularly sensitive

FIG. 4.— IPV10 (crosses) and IPV20 (diamonds) measurements obtained from the Gaussian fits to the line profiles plotted against aperture size as in Figure 3. The Nelson & Whittle (1995) measurements for IPV10 (dotted) and IPV20 (dashed) are plotted as horizontal lines. NGC 7682 is not shown because the red wing of the [S II] line did not fall on the STIS CCD.

to changes in the base and wings of the lines, which may probe the acceleration or deceleration of winds. For example, an increase corresponds to more high-velocity emission-line gas outside of the nuclear region than in the nucleus. While eleven of these galaxies have IPV20 variations of less than 10% between the 0.2″ and 1″ STIS apertures, several exhibit substantial variations. IPV20 increases by over 30% from 0.2″ to 1″ in both MKN 573 and NGC 3227, while it decreases by over 30% for NGC 2110 [O III] (and nearly this amount in [S II]). In contrast, our FW20 measurements for

these galaxies only increase moderately with aperture size, if at all, which implies that the IPV width measurements are indeed more sensitive to behavior in the wings, as was suggested by Whittle (1985a). The substantial IPV decreases with radius in NGC 1358 and NGC 2110 provide good evidence for radiation-driven winds that decelerate at larger scales, as has already been noted for NGC 4151 by Nelson et al. (2000).

We note that several IPV profiles in Figure 4 exhibit pronounced jumps in IPV value with radius between neighboring
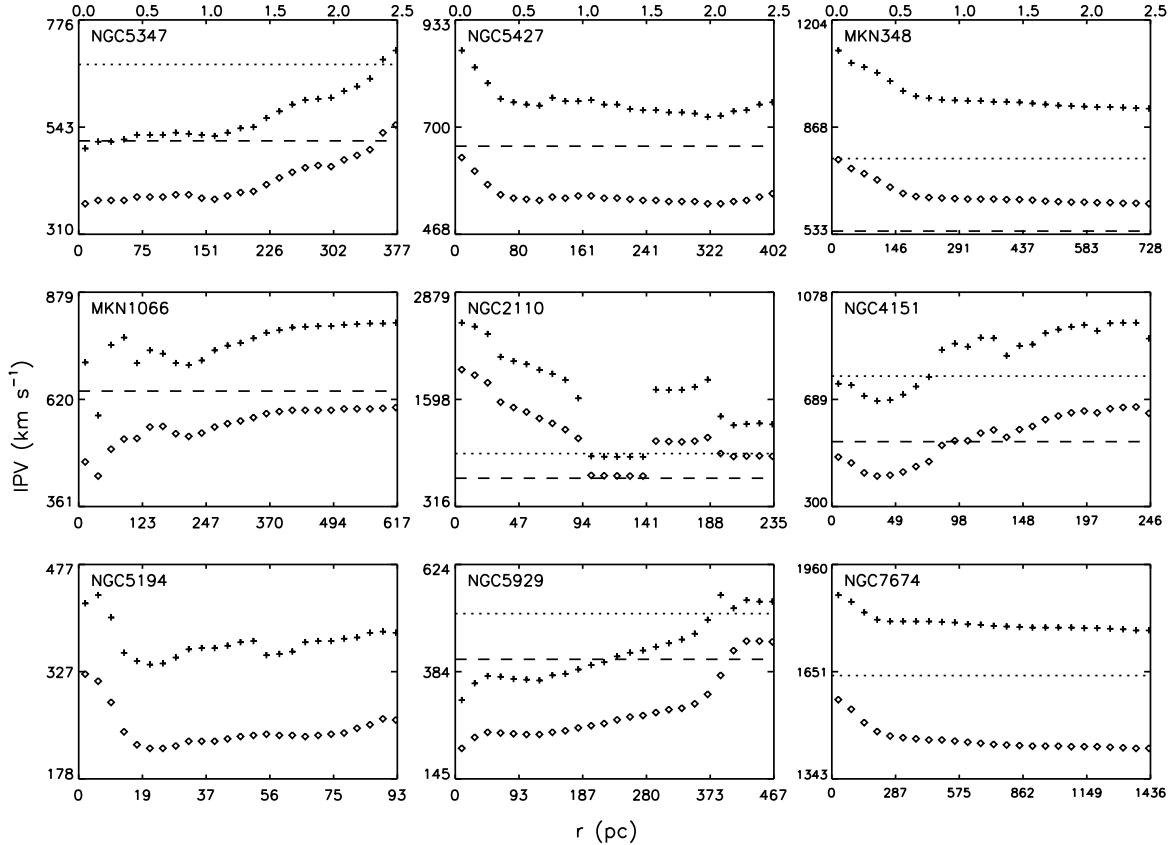
FIG. 4.— *Continued*

data values. These jumps are either due to instances where our Gaussian fitting routine switched between a single-component fit and a multiple-component fit (or vice versa), or the presence of knots of line-emitting gas outside of the nuclear region.

5.2. *Asymmetries*

Figures 3 and 4 described above indicate that markedly different velocity components contribute to the emission-line profiles in the nucleus and at larger scales in approximately half of the sample. In addition to this information on the widths of these velocity components, the presence or absence of asymmetries can provide information on the origin of the line-emitting material along the line of sight, particularly in the presence of significant gas and dust in the NLR.

As noted previously, the [O III] line is quite often reported to have significant, typically blue, asymmetries, while asymmetries are rarely observed in lower-excitation lines (Heckman et al. 1981; de Robertis & Osterbrock 1984; Whittle 1985b). Our measurements of the Whittle (1985b) asymmetry parameters listed in Table 1 confirm that asymmetries are more common in [O III] and these values are illlustrated in Figure 5. Within the 0.2″ aperture we find that 6/7 galaxies with [O III] observations have $|A_{20}| > 0.1$, while 9/18 galaxies with [S II] observations have such asymmetries. While we observe asymmetries less frequently in [S II] than [O III], we still measure asymmetries in a substantially larger fraction of galaxies than typically observed in ground-based observations and we discuss this point further below. Two particularly extreme cases of asymmetries are NGC 1667 [S II] and

NGC 5194 [O III]. The asymmetries are less pronounced in the larger 1″ aperture, where only 7/18 galaxies in the [S II] sample and 5/7 in the [O III] sample have such significant asymmetries.

Several of these galaxies exhibit rather unusual asymmetries. While most have blue asymmetries, several have significant red asymmetries. One peculiar case is MKN 573, which is more asymmetric on larger scales *and* this larger-scale asymmetry is red: $A_{20} = -0.22$ in the 1″ aperture. Inspection of *HST* images of MKN 573 (Martini et al. 2003) reveals that the strong red asymmetry outside of the nucleus is due to the chance intersection of the STIS slit with an individual NLR cloud. MKN 270 [S II], NGC 1667 [S II], and NGC 5194 [O III] also exhibit significant red asymmetries in the 0.2″ aperture spectra, although are less asymmetric on larger scales. The red-asymmetric component in these cases is broader than the core.

Blue asymmetries in [O III] were suggested by Heckman et al. (1981) to be due to a combination of radial outflow from the nuclear region and gas and dust that obscures the red-shifted emission from the far side of the galaxy. The blue asymmetries confined to the nuclear region in NGC 4051, NGC 5347, and MKN 348 agree well with this interpretation. NGC 7682 and MKN 1066 have pronounced asymmetries on larger scales as well (see Figure 1). For these two galaxies 1″ corresponds to several hundred parsecs and would require a large obscuring medium.

We have also investigated the scale-dependence of asymmetries with the spectra shown in the rightmost panels of Figure 1. These spectra are the difference between the spectrum

TABLE 3
IPV WIDTH MEASUREMENTS

Name	—Nelson & Whittle (1995)—			Line	—Aperture = 0.2″—		—Aperture = 1″—		—IPV20—	
	Line	IPV20 (km s^{-1})	IPV10 (km s^{-1})		IPV20 (km s^{-1})	IPV10 (km s^{-1})	IPV20 (km s^{-1})	IPV10 (km s^{-1})	1″/0.2″ (%)	NW95/1″ (%)
(1)	(2)	(3)	(4)	(5)	(6)	(7)	(8)	(9)	(10)	(11)
MKN 270	[O III]	472	637	[S II]	238	371	250	393	5.0	89
MKN 573	[S III]	423	572	[S II]	132	211	196	343	48	120
MKN 686	[O III]	454	593	[S II]	153	273	192	333	25	140
NGC 788	[O III]	225	305	[S II]	104	182	117	191	13	92
NGC 1052	[O III]	810	1075	[S II]	700	961	584	829	-17	39
NGC 1358	[O III]	355	505	[S II]	339	477	254	383	-25	40
NGC 1667	[O III]	365	525	[S II]	549	714	423	549	-23	-14
NGC 2110	[S III]	655	950	[S II]	766	1010	673	907	-12	-3
NGC 2273	[S III]	254	325	[S II]	160	288	189	303	18	34
NGC 3031	[O III]	- - -	- - -	[S II]	441	567	416	537	-5.7	- - -
NGC 3227	[S III]	775	994	[S II]	394	526	546	715	39	42
NGC 3516	[O III]	490	665	[S II]	202	258	221	282	9.4	120
NGC 3982	[O III]	452	452	[S II]	189	324	198	335	4.8	130
NGC 4051	[S III]	293	405	[S II]	224	293	273	351	22	7.3
NGC 4579	[O III]	920	1143	[S II]	586	750	547	704	-6.7	68
NGC 5347	[O III]	513	679	[S II]	236	392	233	395	-1.3	120
NGC 5427	[O III]	659	956	[S II]	299	554	278	518	-7.0	140
NGC 7682	[S III]	266	330	[S II]	774	1102	784	1136	1.3	-66
MKN 348	[O III]	543	770	[O III]	669	991	625	920	-6.6	-13
MKN 1066	[O III]	640	902	[O III]	445	596	545	725	22	17
NGC 2110	[O III]	655	950	[O III]	1670	2199	1105	1640	-33	-41
NGC 4151	[S III]	536	774	[O III]	441	721	533	874	21	0.6
NGC 5194	[S III]	- - -	- - -	[O III]	299	422	232	362	-22	- - -
NGC 5929	[O III]	412	514	[O III]	254	409	261	397	2.8	58
NGC 7674	[O III]	1255	1640	[O III]	1524	1836	1444	1784	-5.2	-13

NOTE. — Col. (1): Galaxy name. Col. (2) Line used for width measurements in NW95. Cols. (3)–(4): IPV20 and IPV10 values given by NW95. Col. (5): Line used for our width measurements. Cols. (6)–(7): IPV20 and IPV10 values for our sample with a 0.″2 aperture. Cols. (8)–(9): IPV20 and IPV10 values for our sample with a 1″ aperture. Col. (10): The percent change in IPV20 from 0.″2 to 1″ aperture sizes. Col. (11): The percent difference between our IPV20 measurement within 1″ and the NW95 IPV20 value.

of each galaxy summed with a $1''$ aperture and a $0.2''$ aperture and therefore effectively isolate the emission-line component due to material outside of the nuclear region. The two vertical lines in each panel for a given galaxy correspond to the line peak of the emission lines in the $1''$ aperture. The line profiles in the rightmost panels relative to these vertical lines therefore illustrate the extent to which emitting material outside of $0.2''$ contributes to any asymmetries in the line profiles. To characterize the line asymmetry outside of the nuclear, $0.2''$ aperture, we calculated the fraction of the total $1'' - 0.2''$ line flux on the blue side of the line centroid in the $1''$ aperture. A fraction greater than 0.5 corresponds to a blue asymmetry, while less than 0.5 corresponds to a red asymmetry. These values are listed in the last column of Table 1. Eight galaxies have strong blue asymmetries outside of $0.2''$ (fraction > 0.6), two have strong red asymmetries (fraction < 0.4), and the remaining 14 are either relatively symmetric (ten) or have little flux outside of $0.2''$ (five) in the STIS aperture. The significant asymmetry in NGC 2110 is only seen in [O III].

6. DISCUSSION

The changes in the NLR velocity field in the STIS aperture have revealed pronounced differences between the unresolved, nuclear kinematics and the NLR on larger scales, yet these larger-scale kinematics still subtend only a fraction of the NLR for many galaxies because of the narrow STIS slit. Even the line characteristics measured from the integrated STIS slit may therefore differ from ground-based flux measurements. We estimated the fraction of the NLR observed

with these observations through a comparison of the total flux in the STIS aperture and the value reported in the ground-based measurements from Whittle (1992a). This comparison demonstrated that the STIS aperture includes between 25% and 90% of the [O III] flux measured by Whittle (1992a) for the seven galaxies with STIS [O III] measurements. The velocity field sampled by the STIS apertures also may depend on the orientation of the spectroscopic slit relative to the major axis of the host galaxies, as there is evidence that rotation is partly responsible for the NLR widths (Whittle 1992b), or the orientation relative to the NLR and radio jet axis, which are known to be unrelated to the host galaxy semimajor axis (Ulvestad & Wilson 1984; Schmitt et al. 2003). However, the orientation for most of these observations were not specified in order to reduce scheduling constraints.

6.1. Comparison with Ground-based Measurements

One striking characteristic of Figures 3 and 4 is how poorly the line profile measurements agree with the ground-based values on even the largest scales (see also Figure 6). Of the 24 galaxies with measured FWHM in the $1''$ aperture, the FWHM of only six (NGC 1358, NGC 3031, NGC 3982, NGC 4051, NGC 4151, and NGC 7674) are within 10% of the ground-based value (see Table 1), while 12 are discrepant by greater than 30% – comparable to the observed scatter in the $\sigma_g - \sigma_*$ correlation. Surprisingly, one of these 12 measurements (NGC 2110 [S II]) is actually $> 30\%$ larger in the STIS aperture than in the ground-based measurement. This broad, nuclear component is quite obvious in Figure 1.

TABLE 4
ASYMMETRY MEASUREMENTS

Name	Line	A10 (0."2) (km s^{-1})	A20 (0."2) (km s^{-1})	A10 (1") (km s^{-1})	A20 (1") (km s^{-1})	Blue Area (1"-0."2) (%)
(1)	(2)	(3)	(4)	(5)	(6)	(7)
MKN 270	[S II]	-0.17	-0.20	-0.12	-0.14	0.43
MKN 573	[S II]	0.00	-0.01	-0.21	-0.22	0.24
MKN 686	[S II]	-0.3	-0.03	0.00	0.00	- - -
NGC 788	[S II]	0.13	0.11	0.03	0.03	0.76
NGC 1052	[S II]	-0.09	-0.09	-0.05	-0.06	0.35
NGC 1358	[S II]	0.01	0.03	0.01	0.01	- - -
NGC 1667	[S II]	-0.23	-0.21	0.03	0.04	0.46
NGC 2110	[S II]	-0.09	-0.10	0.00	0.00	0.48
NGC 2273	[S II]	0.34	0.42	0.34	0.39	0.76
NGC 3031	[S II]	0.00	0.01	0.00	-0.01	0.77
NGC 3227	[S II]	0.09	0.12	0.10	0.13	1.00
NGC 3516	[S II]	0.00	0.01	0.00	0.01	- - -
NGC 3982	[S II]	0.26	0.25	0.24	0.22	- - -
NGC 4051	[S II]	0.29	0.31	0.25	0.25	0.82
NGC 4579	[S II]	-0.06	-0.07	-0.08	-0.09	0.59
NGC 5347	[S II]	0.35	0.37	0.32	0.34	0.56
NGC 5427	[S II]	-0.02	-0.02	-0.02	-0.02	- - -
NGC 7682	[S II]	- - -	- - -	- - -	- - -	0.52
MKN 348	[O III]	0.36	0.38	0.28	0.29	0.56
MKN 1066	[O III]	0.41	0.33	0.31	0.29	0.46
NGC 2110	[O III]	0.15	0.12	0.11	0.14	0.78
NGC 4151	[O III]	-0.02	-0.02	0.14	0.12	0.42
NGC 5194	[O III]	-0.13	-0.18	0.03	0.06	0.52
NGC 5929	[O III]	-0.13	-0.17	-0.08	-0.06	0.70
NGC 7674	[O III]	0.46	0.44	0.45	0.45	0.75

NOTE. — Col. (1): Galaxy name. Col. (2): Emission line used in STIS data analysis. Col. (3) – (4): A20 and A10 asymmetry measurement with an 0.2″ aperture. Col. (5) – (6): A20 and A10 measurement within a 1″ aperture. Col. (7): Fraction of the 1"-0."2 profile area that lies blueward of the 1" line centroid.

For NGC 3516 the difference between the STIS and NW95 measurements can be attributed to the slit orientation as this galaxy is known to have a large, extended NLR (Pogge et al. 1989a), yet we detect little emission in our slit outside of the nuclear region.

For the seven galaxies with [O III] measurements, we examined the difference between the FWHM in our 1″ aperture and the ground-based value as a function of the fraction of the flux within the 1″ STIS aperture. The STIS flux measurement for NGC 7674 includes 90% of the ground-based value reported by Whittle (1992a) and our measured FWHM is within 10% of his value. This confirms that when most of the ground-based flux falls within our much narrower aperture we measure the same kinematics. For the other six galaxies these data miss a larger fraction of the total flux and the line widths are quite different in some instances. The most notable is the STIS measurement of MKN 348, which includes 60% of the ground-based value and is 60% narrower. The STIS measurements of the remaining five galaxies include only 30% of the flux in the Whittle (1992a) aperture and the differences in width between the two aperture sizes range between none (NGC 4151) and 150% (NGC 5929).

The disagreement between widths measured in our 1″ aperture and the ground-based aperture is more striking for IPV20 (see also Table 1) than for line widths as only two galaxies (NGC 4051 and NGC 4151) have STIS 1″ and NW95 measurements that agree within 10%. The majority (15/24) have NW95 values > 30% larger than the STIS measurements and 2/24 (NGC 7682 and NGC 2110 [O III]) are less than 30% of the ground-based measurements. However, we note that most differences in IPV20 between the STIS 1″ and NW95

are comparisons between STIS [S II] and NW95 [O III] measurements and they may therefore partly reflect more pronounced wings in the [O III] line relative to [S II]. For example, NGC 2110 has a 1″ IPV20 = 423 km s^{-1} for [S II] and IPV20 = 1105 km s^{-1} for [O III]. NW95 measured 655 km s^{-1} for [O III].

As described in Section 5.2, there are also substantial differences between the fraction of AGN with asymmetries in the low-excitation [S II] line in these data and ground-based measurements. This change may be due to the dilution of nuclear asymmetries by larger-scale emission from host galaxy starlight or more symmetric emission from the NLR on larger scales. Host galaxy dilution may in particular explain why we detect significant asymmetries in such a large fraction of the [S II] profiles compared to expectations from ground-based programs (Filippenko & Halpern 1984; de Robertis & Osterbrock 1984; Greene & Ho 2005). This result implies that the asymmetries are primarily due to nuclear line-emitting gas, rather than material more evenly distributed throughout the NLR on larger scales.

This comparison of width and IPV values suggest that measurements within the STIS aperture are generally smaller than the ground-based values. A quantitative comparison demonstrates that this is the case, relative to both ground-based NLR width measurements and σ_* (see Table 1 and Figure 6). Comparison of the STIS FWHM measurements in 0.2″, 1″, 100pc, and 200pc apertures (divided by 2.354 to approximate a Gaussian σ_g) to σ_* show that the STIS measurements systematically underestimate σ_* by 10 – 20%. The STIS measurements similarly underestimate the ground-based NW95 FWHM measurements. Figure 6 does not show any signifi-
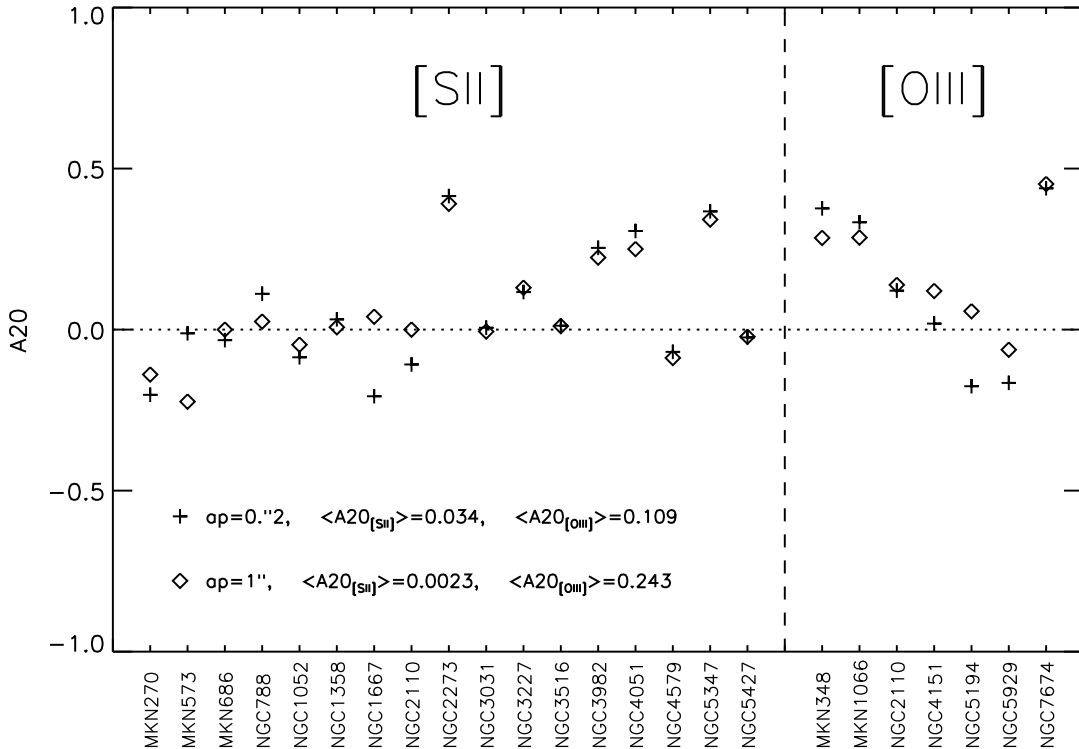
FIG. 5.— A20 measurements for the [S II] and [O III] emission lines in our sample at aperture sizes of $0.2''$ (crosses) and $1''$ (diamonds). Positive A20 values indicate blue asymmetries, negative A20 values indicate red asymmetries, and near-zero values indicate symmetric profiles. The average A20 values for [S II] and [O III] at each aperture are shown.

cant evidence for differences between [S II] and [O III]. The scatter between STIS and σ_* measurements is slightly worse (30 – 40%) than the scatter between STIS and NW95 FWHM measurements (20 – 40%). In contrast, Figure 7 indicates that STIS measurements at $0.2''$ and $1''$ and 100pc and 200pc are significantly more similar in value and have substantially less scatter (10 – 20%, see also Table 1). The smaller measured widths in the STIS slit is likely due to the collisional nature of gas, which will therefore tend to reside at least partially in a disk. A narrow slit at a random orientation will then sample a smaller fraction of the full radial velocity field than a larger aperture slit and therefore measure a smaller width.

The comparable number of galaxies with red and blue asymmetries on larger scales, and more importantly that these asymmetries are in general substantially weaker than those in the $0.2''$ aperture, suggest that asymmetries measured in large (including ground-based) apertures originate on small scales, or less than ~ 100pc based on the spatial resolution of these observations.

6.2. *Correlations with Global Properties*

In addition to the quality of the correlations between line widths measured in various apertures and σ_*, we also searched for systematic trends between the residuals and the properties of the galaxies. We specifically investigated the residuals between the measurements in the $1''$ aperture and σ_* as a function of distance, Hubble type, fraction of the galaxy in a $1''$ aperture, and radio power. Significant residuals as a function of galaxy distance, Hubble type, and fraction of the angular size of the galaxy subtended by the spectroscopic slit would indicate very useful information about the origin of the scatter in the $\sigma_g - \sigma_*$ relation and these quantities could poten-

tially be used to empirically determine corrections to reduce scatter, as well as provide insight into its origin. For example, the NLR measured exactly within the host bulge's effective radius might prove to be the best tracer of σ_*. Some evidence for such a relation might be revealed in the residuals plotted against these three parameters, however as shown in Figure 8 there is no evidence that the residuals are correlated with any of these parameters.

Whittle (1992c) found evidence that Seyfert galaxies with linear radio morphology and high luminosity tend to have broader lines. We do not see significant correlation between residuals in $\sigma_g - \sigma_*$ in our data, although only three galaxies in our sample are above his radio luminosity threshold of $L_{1415} \geq 10^{22.5}$ W Hz^{-1}. Other parameters mentioned in the Introduction that correlate with systematically broader emission-line widths include L/L_{Edd} (Greene & Ho 2005) and disturbed morphologies (Whittle 1992b), however this sample does not contain a sufficient number of objects with either high accretion-rates or significantly-disturbed morphologies to investigate these quantities. Boroson (2005) also recently noted that strongly blueshifted [O III] lines (relative to the host galaxy) were systematically broader than similar objects that were not blueshifted. These objects tended to be those with large L/L_{Edd}. None of the seven galaxies in our [O III] sample have substantial blueshifts.

7. SUMMARY

We have conducted a detailed analysis of spatially-resolved [O III] and [S II] NLR emission from 24 well-studied, nearby AGN. These observations have detected considerable emission outside of the unresolved nucleus ($0.2''$ or 10 – 100pc) and this emission often contributes significantly to the mea-
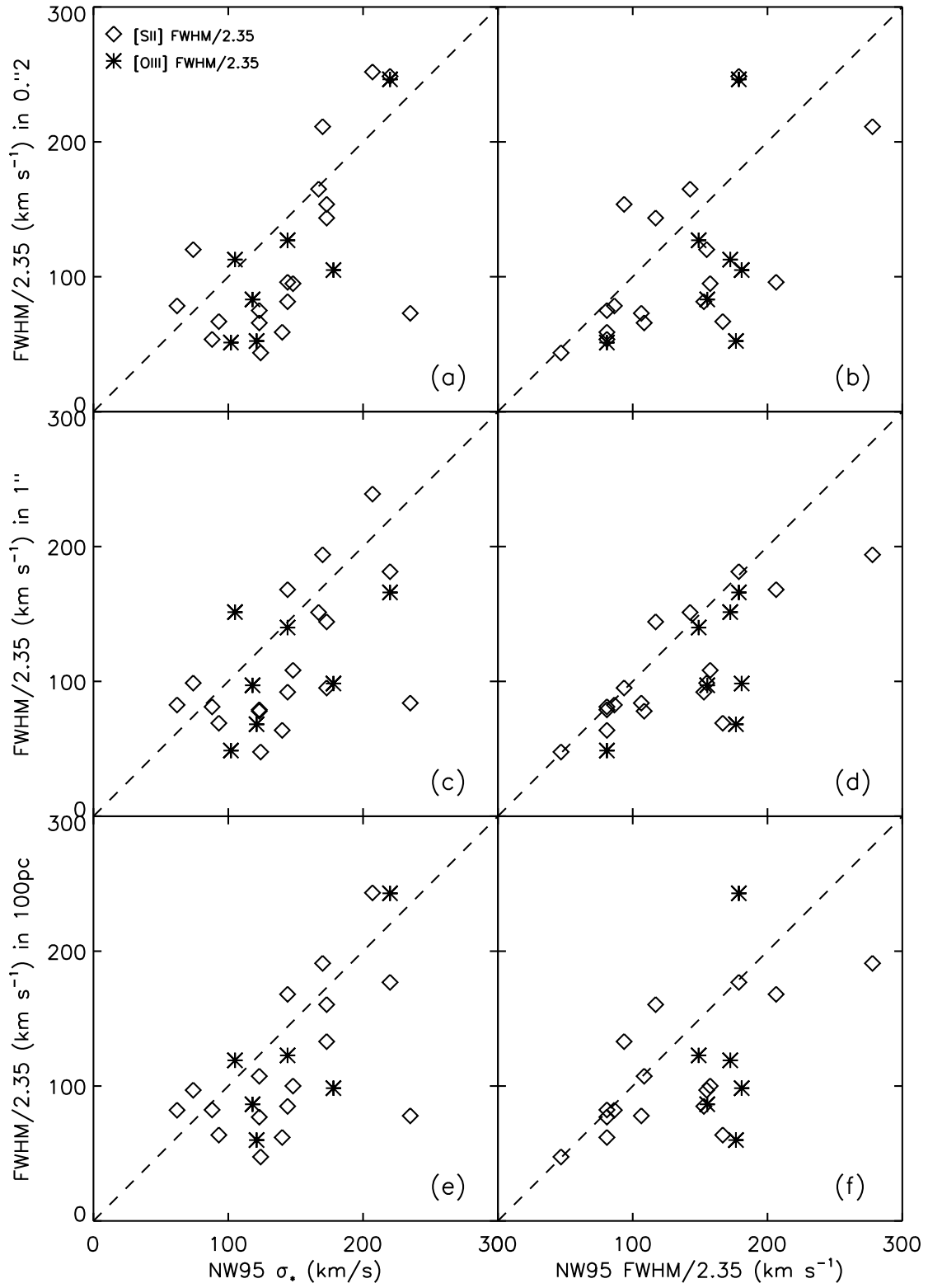
FIG. 6.— Our measurements of FWHM/2.354 plotted against NW95 σ_* (left panels) and NW95 FWHM/2.354 (right panels). The top panels (a & b) show our [S II] (diamond) and [O III] (star) FWHM measurements in an 0.2″ aperture, the middle two panels show our measurements in a 1″ aperture, and the bottom two panels show our measurements in a fixed physical aperture size of 100pc. The dashed line in each frame represents a 1:1 correspondence between the quantities plotted.

TABLE 5
STATISTICAL RESULTS

(1)	Aperture Size (2)	[S II] (km s^{-1}) (3)	[O III] (km s^{-1}) (4)	Total (km s^{-1}) (5)
$\langle$(FWHM/2.354)/$\sigma_*\rangle$	0."2	0.81 ± 0.36	0.76 ± 0.11	0.80 ± 0.34
	1"	0.82 ± 0.31	0.80 ± 0.33	0.81 ± 0.31
	100pc	0.83 ± 0.31	0.81 ± 0.27	0.83 ± 0.30
	200pc	0.85 ± 0.30	0.83 ± 0.30	0.84 ± 0.29
$\langle$FWHM/NW95 FWHM$\rangle$	0."2	0.84 ± 0.33	0.70 ± 0.34	0.80 ± 0.33
	1"	0.84 ± 0.20	0.70 ± 0.22	0.80 ± 0.21
	100pc	0.86 ± 0.27	0.72 ± 0.35	0.82 ± 0.29
	200pc	0.88 ± 0.24	0.70 ± 0.21	0.83 ± 0.24
$\langle$FWHM/FWHM$\rangle$	1" / 0."2	1.06 ± 0.26	1.07 ± 0.23	1.06 ± 0.25
	200pc / 100pc	1.03 ± 0.10	1.04 ± 0.20	1.03 ± 0.13
$\langle$(NW95 FWHM/2.354)/$\sigma_*\rangle$		- - -	1.15 ± 0.33	- - -

NOTE. — Col. (1): Pair of values used for statistical comparison. Col. (2): Aperture size used in our measurement of FWHM/2.354. Col. (3): Mean and standard deviation of the sources for which we measure the [S II] line widths. Col. (4): Mean and standard deviation of the sources for which we measure the [O III] line widths. Col. (5): Mean and standard deviation of all sources.
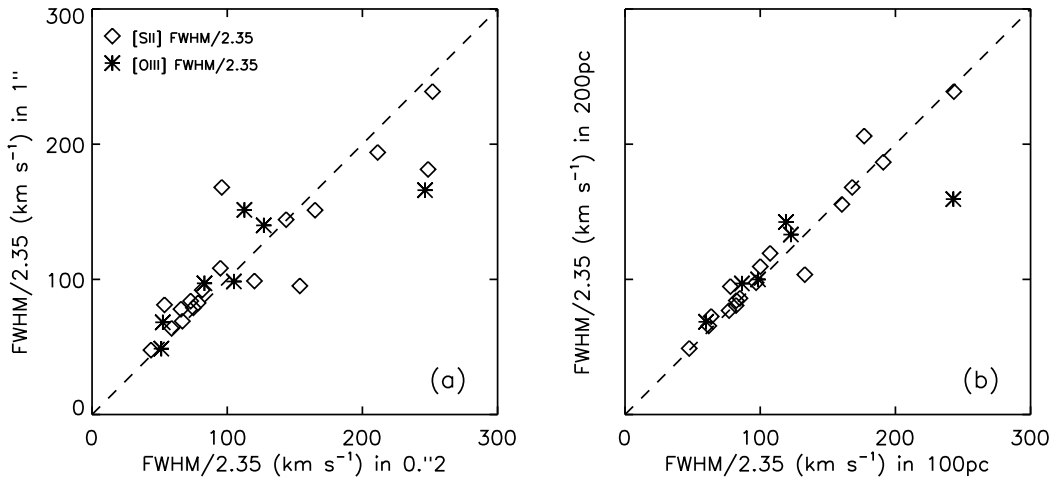

FIG. 7.— Comparison of our [S II] (diamonds) and [O III] (stars) FWHM measurements in different apertures. (a) Width measured in a 1″ aperture plotted against the width measured in an 0.2″ aperture. (b) Width measured in a 200pc aperture plotted against the width measured in a 100pc aperture. The dashed line in each frame represents a 1:1 correspondence between the quantities plotted.
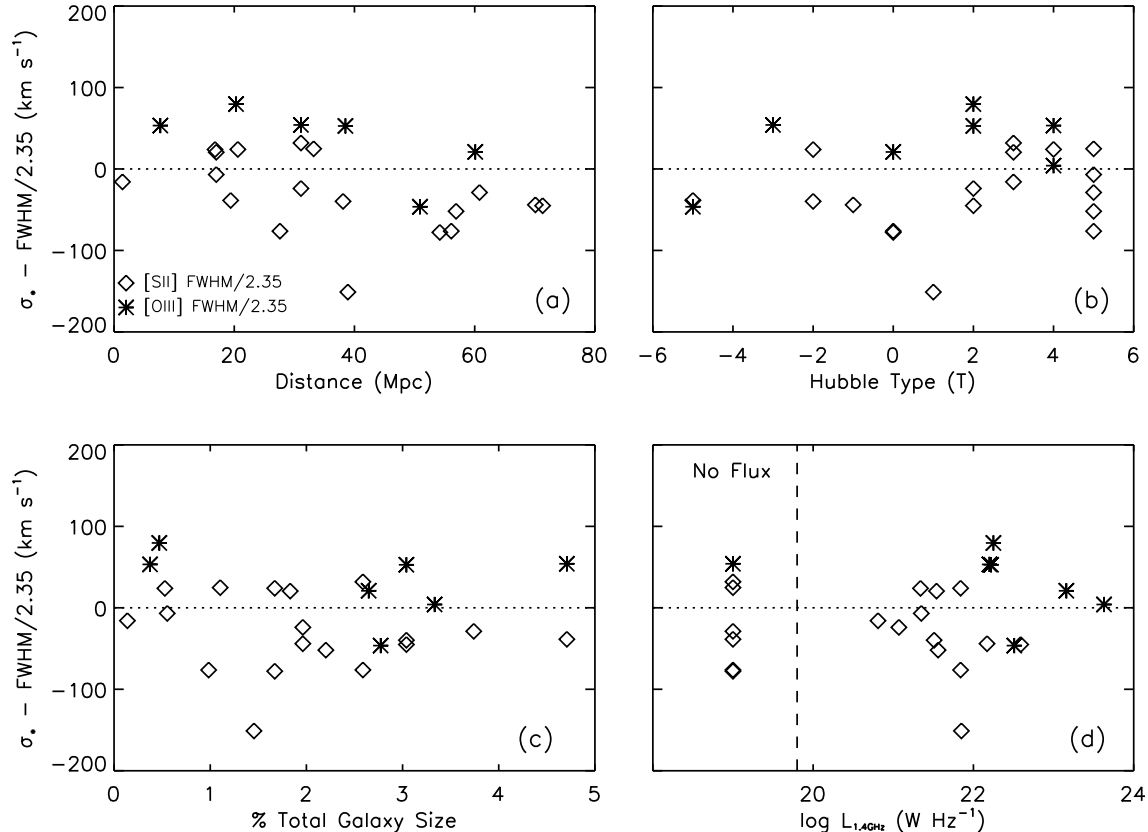
FIG. 8.— Comparison of residuals between gas and stellar kinematics and various global properties. The four panels show: (a) Distance; (b) Hubble T type; (c) Fraction of the galaxy size (2″ divided by the angular size provided in Table 1); and (d) radio power. The points to the left of the dashed line do not have a measured radio flux and are only shown to indicate the ordinate values.

sured line profiles at larger scales. We have characterized the spatial dependence of this emission with a range of width, area, and asymmetry measurements and shown there are not only substantial changes from 0.2″ to 1″ (typical of ground-based observations), but also from a 1″ long STIS aperture (with either a 0.1″ or 0.2″ width) and the approximately 1″ × 1″ or larger aperture used for ground-based measurements of these galaxies. In particular, the large variations in line profiles as a function of aperture size demonstrates that the profile of the NLR lines are set by the kinematics of the gas in the NLR itself, and not just radiatively-driven winds from the nucleus.

The spatial scale(s) responsible for the NLR emission lines has received substantial recent attention because the widths of the NLR lines may be used to estimate the stellar velocity dispersion σ_*, which in turn can be used as a proxy for the black hole mass $M_\bullet$. Our analysis shows that even at the largest spatial scales observed with STIS, the line widths are systematically smaller by $10-20\%$ than ground-based width measurements (as well as σ_*). As we estimate that the STIS slit may include as little as 25% of the NLR flux, emission on larger scales or outside of the narrow STIS slit width must broaden the line profiles.

While the line profile measurements from the STIS data are systematically less than the ground-based NLR and σ_* values, the scatter is comparable. The substantial scatter in the $\sigma_g - \sigma_*$ relation therefore appears to be due to a sufficiently complex set of parameters that it is effectively stochastic, at least to the extent that the scatter can not be reduced to the magnitude of the scatter in the $M_\bullet - \sigma_*$ relation. In addition to rotation,

Eddington ratio, and compact radio jets, the list of parameters that increase the scatter should include the clumpiness of the NLR, the orientation of the NLR with respect to the host galaxy semimajor axis, and the amount and distribution of dust in the NLR. If the NLR were as isotropic as the stellar distribution, the scatter would be comparable to the $M_\bullet - \sigma_*$ relation, yet because the gas is collisional, and also clumpy, it can not be as good a tracer of the bulge potential.

This interpretation is supported by the substantial and diverse types of width variations observed in these spatially-resolved measurements. Specifically, the most common types of line width variation are $< 30\%$ changes between the 0.2″, 1″, and NW95 apertures (nine galaxies) and relatively little width increase in the STIS aperture, but a substantial increase ($> 30\%$) between the 1″ STIS and NW95 measurements (also nine galaxies). The remaining types of variations observed are greater than 30% width changes on the STIS scales only (four) and on all scales (two). Two of the four galaxies with only substantial profiles changes on the STIS scale have substantially broader emission in the 0.2″ than in the 1″ aperture. These large nuclear velocities may be due to radiatively-driven winds that decelerate or simply do not extend to larger scales. However, neither of these nuclear line profiles exhibit substantial asymmetries, which suggests that if this emission is due to a uniform outflow, there is not substantial dust in the nuclear region.

Both red and blue asymmetries are observed in the [S II] and [O III] line profiles. These observations are unusual in two respects. First, asymmetries in [S II] are reported far less frequently than in [O III], yet we observe [S II] asymmetries with

nearly comparable frequency. The low frequency of observed [S II] asymmetries in ground-based observations have been ascribed to the fact that [S II] is a lower-ionization line. Our observations suggest that asymmetries are commonly present in [S II], but the weaker [S II] emission is more easily diluted by host galaxy starlight and not as readily observed in the larger ground-based apertures. Secondly, we observe several examples of galaxies with red asymmetries in either [S II] or [O III]. For the cases in which the red asymmetries are largely confined to the unresolved nuclear spectrum, these observations do not agree well with outflow models that produce blue asymmetries through invocation of obscuration of the far side of the galaxy. These red asymmetries may be due to the patchy nature of the ISM on very small scales, which may produce uneven illumination of NLR clouds and a patchy line-of-sight velocity distribution for the NLR clouds. Such variations within the NLR may be responsible for the bulk of the scatter in the $\sigma_g - \sigma_*$ correlation.

REFERENCES

Barth, A.J., Ho, L.C., Filippenko, A.V., 2001, ApJ, 546, 205

Boroson, T. 2003, ApJ, 585, 647

Boroson, T. 2005, AJ, *in press*

Crenshaw, D.M. & Kraemer, S.B. 2000, ApJ, 532, L101

Condon, J. J., Cotton, W. D., & Broderick, J. J. 2002, AJ, 124, 675

Das, V. et al. 2005, AJ, *in press*

Ferrarese, L., & Merrit, D. 2000, ApJ, 539, L9

Ferrarese, L., Pogge, R.W., Peterson, B.M., Merritt, D., Wandel, A., & Joseph, C.L. 2001, ApJ, 555, L79

Filippenko, A.V. & Halpern, J.P. 1984, ApJ, 285, 458

Gebhardt, K., Bender, R., Bower, G., Dressler, A., Faber, S. M., Filippenko, V., Green, R., Grillmair, C., Ho, L. C., Kormendy, J., Lauer, T. R., Magorrian, J., Pinkney, J., Richstone, D., & Tremaine, S. 2000a, ApJ, 539, L13

Gebhardt, K., Bender, R., Bower, G., Dressler, A., Faber, S. M., Filippenko, V., Green, R., Grillmair, C., Ho, L. C., Kormendy, J., Lauer, T. R., Magorrian, J., Pinkney, J., Richstone, D., & Tremaine, S. 2000b, ApJ, 543, L5

Greene, J. E., & Ho, L. C. 2005, ApJ, *in press*

Grupe, D. & Mathur, S. 2004, ApJ, 606, L41

Heckman, T. M., Miley, G. K., van Breugel, W. J. M., & Butcher, H. R. 1981, ApJ, 247, 403

Ho, L.C. & Peng, C.Y. 2001, ApJ, 5555, 650

Jensen, J.B. et al. 2003, ApJ, 583, 712

Krolik, J. H., & Vrtilek, J. M. 1984, ApJ, 279, 521

Kaspi, S., Smith, P.S., Netzer, H., Maoz, D., Jannuzi, B.T., & Giveon, U. 2000, ApJ, 533, 631

Martini, P., Regan, M.W., Mulchaey, J.S., & Pogge, R.W. 2003, ApJS, 146, 353

Nelson, C. H., & Whittle, M. 1995, ApJS, 99, 67

Nelson, C. H., & Whittle, M. 1996, ApJ, 465, 96

Nelson, C. H. 2000, ApJ, 544, L91

Nelson, C. H. et al. 2000, ApJ, 531, 257

Nelson, C. H., Plasek, A., Thompson, A., Gelderman, R., & Monroe, T. 2004, AGN Physics with the Sloan Digital Sky Survey, G. Richards and P. Hall, ASP Conference Series, 311, 83

Nilson, P. 1973, Uppsala General Catalog of Galaxies, (Uppsala: Roy Soc Sci Uppsala)

Onken, C.A., Ferrarese, L., Merritt, D., Peterson, B.M., Pogge, R.W., Vestergaard, M., & Wandel, A. 2004, ApJ, 615, 645

Pogge, R. W. 1989a, AJ, 98, 124

Pogge, R. W. 1989b, ApJ, 345, 730

de Robertis, M. M., & Osterbrock, D. E. 1984, ApJ, 286, 171

de Robertis, M. M.,& Osterbrock, D. E. 1986, ApJ, 301, 727

Robertson, B. et al. 2005, ApJ, *submitted*

Schiano, A.V.R. 1986, ApJ, 302, 95

Schmitt, H.R., Donley, J.L., Antonucci, R.R.J, Hutchings, J.B., Kinney, A.L., & Pringle, J.E. 2003, ApJ, 597, 768

Shields, G. A. et al. 2003, ApJ, 583, 124

Shields, J. C., Rix, H. -W., Barth, A. J., Filippenko, A. V., Ho, L. C., McIntosh, D. H., Rudnick, G., Sargent, W. L. W., & Sarzi, M. 2005, ApJ, *submitted*

Shuder, J. M., & Osterbrock, D. E. 1981, ApJ, 250, 55

Smith, S.J. 1993, ApJ, 411, 570

Solanes, J.M., Sanchis, T., Salvador-Solé, E., Giovanelli, R., & Haynes, M.P. 2002, AJ, 124, 2440

Tremaine, S. et al. 2002, ApJ, 574, 740

Tully, R.B. 1988, Nearby Galaxies Catalog (Cambridge: Cambridge Univ. Press)

Ulvestad, J.S. & Wilson, A.S. 1984, ApJ, 285, 439

van Dokkum, P. G. 2001, PASP, 113, 1420

de Vaucouleurs, G., de Vaucouleurs, A., Corwin, H. G., Jr., Buta, R. J., Paturel, G., & Fouqué, P. 1991, The Third Reference Catalog of Bright Galaxies, Vol 1-3, (New York: Springer-Verlag)

Vorontsov-Velyaminov, B. A., & Arkipova, V. P. 1974, Morphological Catalogue of Galaxies, V, Moscow State University

Whittle, M. 1985a, MNRAS, 213, 1

Whittle, M. 1985b, MNRAS, 213, 33

Whittle, M. 1992a, ApJS, 79, 49

Whittle, M. 1992b, ApJ, 387, 109

Whittle, M. 1992c, ApJ, 387, 121